

Protection Study of MTDC Power System

Vishnu Sai Nair

Delft University of Technology

Protection Study of MTDC Power System

by

Vishnu Sai Nair

to obtain the degree of Master of Science in Sustainable Energy Technology at the Delft University of Technology, to be defended publicly on 15 December, 2023.

Student Number: 5505976
Project Duration: December 13, 2022 - November 26, 2023
Thesis Committee: Prof. Marjan Popov, TU Delft, Supervisor
Prof. Aleksandra Lekić, TU Delft, Supervisor
Prof. Aditya Shkehar, TU Delft
Research Group: Intelligent Electrical Power Grids
Faculty: Faculty of Electrical Engineering, Mathematics and Computer Science, Delft

Cover image URL: <https://sciencing.com/ac-dc-electricity-6465233.html>

Acknowledgements

I would first like to thank my thesis supervisors Professor Marjan Popov and Professor Aleksandra Lekić for having provided me with the opportunity to do a thesis on HVDC protection and their constant support and guidance. Furthermore, I would like to thank my daily supervisor Le Liu for introducing me to the field of research in HVDC protection and guiding me towards the development of my thesis on a regular basis. His efforts have been crucial to the completion of this thesis. Lastly, I would like to thank my family and friends for the unwavering mental and emotional support they have provided over these last two years.

Vishnu Sai Nair
Delft, December 2023

Summary

This thesis investigates and compares the performance of HVDC protection algorithms in terms of their sensitivity, selectivity, speed, and robustness. The threshold determination process for each algorithm has been described in detail as well. Each algorithm is tested under various fault resistances, and fault distances to test the sensitivity of the algorithm. The trip time for each case in each algorithm is monitored to analyze the speed of the algorithm. Various external faults have been simulated to test the selectivity of the algorithm. Lastly, the resilience of each algorithm against white noise has been tested. Furthermore, the effect of varying the sampling frequency and the inductance of the current limiting inductors on each algorithm is investigated. The HVDC protection algorithms discussed are - current differential deviation-based protection, ROCOV-based protection, ROCOC-based protection, and DC reactor voltage change rate-based protection. All protection algorithms have been implemented in the PSCAD environment. The noise resilience analysis for each algorithm has been performed in MATLAB.

List of Figures

1.1	Cost comparison of HVAC and HVDC transmission. [1]	3
1.2	The fault current path of an IGBT-based two-level converter during a fault (for one phase) [59]	4
1.3	Categories of protection philosophies [32]	4
2.1	Test DC System	8
2.2	MMC Structure [24]	9
4.1	Data acquisition for current differential deviation-based protection	17
4.2	Logic scheme for current differential deviation-based protection	18
4.3	MMC with terminal inductors [25]	18
4.4	Inductor voltage-based algorithm flowchart	19
4.5	Simplified section of the 4 terminal CIGRE B4.57 model	19
4.6	V_{p31} during internal faults	20
4.7	$ROCOV_P$ for internal faults	20
4.8	V_{p31} during external faults	20
4.9	$ROCOV_P$ for external faults	21
4.10	ROCOV-based algorithm flowchart	21
4.11	Simplified section of the 4 terminal CIGRE B4.57 model	21
4.12	Current measurements for ROCOC-based protection	22
4.13	I_{p31} during internal faults	22
4.14	$ROCOCP$ during internal faults	22
4.15	I_{p31} during external faults	23
4.16	$ROCOCP$ during external faults	23
4.17	ROCOV-based algorithm flowchart	23
5.1	Input signals for HVDC protection algorithm	24
5.2	Various faults simulated in the HVDC test system	26
5.3	$\Delta \frac{dI_p}{dt}$ for internal faults	26
5.4	$\Delta \frac{dI_n}{dt}$ for internal faults	27
5.5	Breaker status for internal faults	27
5.6	$\Delta \frac{dI_p}{dt}$ for external faults	29
5.7	$\Delta \frac{dI_n}{dt}$ for external faults	29
5.8	Breaker status for external faults	30
5.9	$\Delta \frac{dI_p}{dt}$ for a PTG fault with varying terminal inductance	30
5.10	I_{p13} with 40dB noise	31
5.11	I_{p31} with 40dB noise	31
5.12	$\Delta \frac{dI_p}{dt}$ with 40 dB noise	31
5.13	$ROCOV_P$ for internal faults	33
5.14	$ROCOV_N$ for internal faults	33
5.15	Breaker operation for internal faults	33
5.16	$ROCOV_P$ for external faults	35
5.17	$ROCOV_N$ for external faults	35
5.18	Breaker operation for external faults	36
5.19	V_{p31} with 40 dB noise	36
5.20	$ROCOV_P$ with 40 dB noise	37
5.21	$ROCOCP$ for internal faults	38
5.22	$ROCOCP$ for internal faults	38
5.23	Breaker operation for internal faults	39

5.24 $ROCOCP$ for external faults	40
5.25 $ROCOCN$ for external faults	41
5.26 Breaker operation for external faults	41
5.27 $ROCOCP$ during internal faults with varied terminal inductance	41
5.28 Ip_{31} with 40 dB noise	42
5.29 $ROCOCP$ with 40 dB noise	42
5.30 V_{LT} for internal faults	44
5.31 Breaker operation for internal faults	44
5.32 V_{LT} for external faults	46
5.33 Breaker operation for external faults	46
5.34 V_{LT} during internal faults with varied terminal inductance	47
5.35 V_{LT} with 40 dB noise	47

List of Tables

1.1	HVDC projects installed across the world [10]	2
3.1	Summary of non-unit HVDC protection algorithms	16
5.1	Effect of fault resistance on Current Differential Deviation-based protection	28
5.2	Effect of fault distance on Current Differential Deviation based protection	28
5.3	Effect of external faults on Current Differential Deviation-based protection	29
5.4	Effect of inductance on Current Differential Deviation-based protection	30
5.5	Threshold determination of Current Differential Deviation-based protection	32
5.6	Effect of sampling frequency on Current Differential Deviation-based protection	32
5.7	Effect of fault resistance on ROCOV-based protection	34
5.8	Effect of fault distance on ROCOV-based protection	34
5.9	Effect of external faults on ROCOV-based protection	35
5.10	Effect of inductance on ROCOV-based protection	36
5.11	Threshold determination of ROCOV-based protection	37
5.12	Effect of sampling frequency on ROCOV-based protection	38
5.13	Effect of fault resistance on ROCOC-based protection	39
5.14	Effect of fault distance on ROCOC-based protection	40
5.15	Effect of external faults on ROCOC-based protection	40
5.16	Effect of inductance on ROCOC-based protection	42
5.17	Threshold determination of ROCOC-based protection	43
5.18	Effect of sampling frequency on ROCOC-based protection	43
5.19	Effect of fault resistance on DC Reactor Voltage Change Rate-based protection	45
5.20	Effect of fault distance on DC Reactor Voltage Change Rate-based protection	45
5.21	Effect of external faults on DC Reactor Voltage Change Rate-based protection	46
5.22	Effect of inductance on DC Reactor Voltage Change Rate-based protection	47
5.23	Effect of sampling frequency on DC Reactor Voltage Change Rate-based protection	48
6.1	HVDC protection performance summary	52

List of Acronyms

Acronym	Definition
AC	Alternating current
ACCB	AC circuit breakers
ANFIS	Adaptive neuro-fuzzy inference system
ANN	Artificial neural network
DC	Direct current
DCCB	DC circuit breakers
DFT	Discrete Fourier transform
FB	Full-bridge
FFT	Fast Fourier transform
FT	Fourier transform
GTO	Gate turn-off thyristors
HB	Half-bridge
HHT	Hilbert-Huang transform
HIF	High impedance fault
HVDC	High voltage DC
IGBT	Insulated gate bipolar transistors
LCC	Line-commutated converters
MMC	Modular multilevel converter
MTDC	Multi-terminal DC
NTG	Negative pole-to-ground
PTG	Positive pole-to-ground
PTP	Pole-to-pole
PWM	Pulse width modulation
ROCOC	Rate of change of current
ROCOV	Rate of change of voltage
SM	Sub-module
ST	Stockwell transform
STFT	Short time Fourier transform
SVM	Support vector machine
SWT	Stationary wavelet transform
TE	Transient energy
TW	Traveling wave
VSC	Voltage source converter
WT	Wavelet transform
WTMM	Wavelet transform modulus maximum

Contents

1	Introduction	1
1.1	Background	1
1.2	Benefits of HVDC systems	2
1.3	Motivation	3
1.4	Research Questions	5
1.4.1	HOW CAN DC FAULTS BE DETECTED IN A FAST AND ACCURATE WAY?	5
1.4.2	HOW CAN THE PROTECTION'S SELECTIVITY BE ENSURED?	5
1.5	Research Objectives	5
1.6	Outline of Thesis	6
2	A VSC-HVDC Grid Based Test System	8
2.1	Introduction	8
2.2	MMC	9
2.3	Terminal Inductors	9
3	State-of-the-Art HVDC Protection Algorithms	11
3.1	Introduction	11
3.2	Unit Protection Algorithms	11
3.2.1	Current Differential Protection:	12
3.2.2	Directional Protection:	12
3.3	Non-Unit Protection Algorithms	13
3.3.1	Overcurrent and Undervoltage-Based Algorithms -	13
3.3.2	Current and Voltage Derivative-Based Algorithms -	13
3.3.3	Terminal Inductor-Based Algorithms -	14
3.3.4	Time-Domain TW-Based Algorithms -	14
3.3.5	Frequency Domain-Based Algorithms	14
4	Examined Protection Algorithms	17
4.1	Introduction	17
4.2	Current Differential Deviation	17
4.3	DC Reactor Voltage Change Rate	18
4.4	ROCOV	19
4.5	ROCOC	21
5	Results	24
5.1	Introduction	24
5.2	Current Differential Deviation	26
5.2.1	Effect of Internal Fault Cases	26
5.2.2	Effect of Fault Resistance	27
5.2.3	Effect of Fault Distance	27
5.2.4	Effect of External Fault Cases	29
5.2.5	Effect of Terminal Inductor Inductance	30
5.2.6	Influence Of Noise on Protection Performance	30
5.2.7	Threshold Design	31
5.2.8	Effect of Sampling Frequency	32
5.3	ROCOV	32
5.3.1	Effect of Internal Fault Cases	32
5.3.2	Effect of Fault Resistance	33
5.3.3	Effect of Fault Distance	34
5.3.4	Effect of External Fault Cases	34
5.3.5	Effect of Terminal Inductor Inductance	36

5.3.6	Influence Of Noise on Protection Performance	36
5.3.7	Threshold Design	37
5.3.8	Effect of Sampling Frequency	37
5.4	ROCOC	38
5.4.1	Effect of Internal Fault Cases	38
5.4.2	Effect of Fault Resistance	39
5.4.3	Effect of Fault Distance	39
5.4.4	Effect of External Fault Cases	40
5.4.5	Effect of Terminal Inductor Inductance	41
5.4.6	Influence Of Noise on Protection Performance	42
5.4.7	Threshold Design	42
5.4.8	Effect of Sampling Frequency	43
5.5	DC Reactor Voltage Change Rate	43
5.5.1	Effect of Internal Fault Cases	43
5.5.2	Effect of Fault Resistance	44
5.5.3	Effect of Fault Distance	44
5.5.4	Effect of External Fault Cases	45
5.5.5	Effect of Terminal Inductor Inductance	46
5.5.6	Influence Of Noise on Protection Performance	47
5.5.7	Threshold Design	47
5.5.8	Effect of Sampling Frequency	48
6	Comparison and Analysis	49
6.1	Summary of HVDC Protection Algorithms Performance	49
6.1.1	Current Differential Deviation	49
6.1.2	ROCOV	49
6.1.3	ROCOC	50
6.1.4	DC Reactor Voltage Change Rate	51
6.2	Inferences	51
7	Conclusion and Future Work	53
7.0.1	Conclusion	53
7.0.2	Future Work	54
	References	55

1

Introduction

1.1. Background

Modern power transmission utilizes alternating current (AC) systems to transfer electrical power owing to the easy transformation of voltage levels using transformers. Thus, electricity could be delivered over long distances with low losses. Furthermore, because of the simpler and cheaper AC generators and motors, the use of AC systems became widespread globally [19]. However, since the invention of line-commutated converters (LCC) and due to their ability to achieve high power and voltage ratings with simpler complexity and compact size, High Voltage Direct Current (HVDC) transmission has become a front-runner in the research field of power transmission.

In recent years, HVDC technology has significantly improved as a result of controllable power electronic devices such as gate turn-off thyristors (GTO) and insulated-gate bipolar transistors (IGBT). These devices gave rise to a novel concept of AC/DC converters which are known as voltage source converters (VSCs). Unlike LCCs, VSCs can realize local control of active power and reactive power, or AC and DC voltages due to their ability to be turned off. Furthermore, VSC-HVDC systems have no commutation failure whereas LCC inverters may suffer commutation failure during AC faults [58].

The VSC can be further classified as a two-level converter, a three-level converter, and a modular multilevel converter (MMC) based on the configuration of the power electronic devices. The MMC configuration has lower losses than the two and three-level configurations due to the implementation of modulation techniques such as step firing pulse width modulation (PWM) and shifted-carrier PWM [5, 15]. Additionally, because a direct series connection of IGBTs or GTOs is not necessary, the MMC does not need gate drives as sophisticated as those of the two and three-level converters. This makes the prospect of using the MMC configuration for VSCs very attractive.

Over the past few years, several HVDC projects have been established across the world, including the North Sea projects of BorWin, DoIWin, and NorNed, and the projects of Zhoushan, Wudongde, and Zhangbei in China. Table 1.1 summarizes some of the HVDC projects that have been installed in different regions of the world.

Project	Power (MW)	Voltage (kV)	Line Length (km)	Country
Three Gorges–Shanghai	3000	± 500	1060	China
NorNed	700	± 450	580	Netherlands-Norway
SAPEI	1000	± 500	435	Italy
Mundra–Haryana	2500	± 500	960	India
DolWin2	900	± 320	135	Germany
Western HVDC Link	2200	± 600	422	UK
NordBalt	700	± 300	450	Sweden-Lithuania
Yunnan–Guangdong	5000	± 800	1418	China
BorWin1	400	± 150	200	Germany
Estlink	3000	± 500	1060	Estonia–Finland

Table 1.1: HVDC projects installed across the world [10]

1.2. Benefits of HVDC systems

The transition to HVDC technology comes with many challenges, such as the construction of converter stations, equipment maintenance, and long-term configuration of the transmission line system. Furthermore, factors such as the environmental impact of implementing HVDC technology need to be taken into consideration. However, the advantages of HVDC technology make this transition widely acceptable. When compared to traditional AC systems, HVDC systems, particularly VSC-based HVDC systems, have the following advantages -

- **Higher efficiency** - In AC systems, power is transmitted through periodic voltage and current waveforms with a fixed frequency (50Hz or 60Hz). Due to the phase difference between the voltage and current waveforms, reactive power transfer takes up a part of the transmission line capacity. This is considered a loss in the transmission system as reactive power does not contribute to the power transfer taking place through the transmission line.

The reactive power, when flowing in a long-distance AC transmission line, becomes extremely high. This reactive power flow reduces AC voltage stability; thus, an excessively long transmission line or cable jeopardizes the power quality within an AC system. Additionally, AC exhibits the “skin effect”, i.e. it flows through a path that is close to the surface of a conductor. This results in the increase of the equivalent resistance of a conductor and thus, a greater power loss.

In contrast, there is no periodic change in DC voltage and current. This implies that no reactive power is generated. Furthermore, due to the absence of the “skin effect”, the power losses in DC transmission are lower as compared to its AC counterpart, thus making HVDC transmission a more favorable alternative to transmitting electrical power over long distances.

- **Interconnection of asynchronous AC systems** - AC systems operate on typically two frequencies globally: 50Hz and 60Hz. The choice of system frequency varies from one country to another and it is impossible to directly link two AC systems having different frequencies as such a connection would result in the collapse of both systems. This interconnection can be achieved through the use of back-to-back HVDC stations. Two instances of such an interconnection can be found in the Rivera back-to-back HVDC link which connects Uruguay (50Hz) and Brazil (60Hz) [35] and the back-to-back system linking the western (60Hz) and eastern (50Hz) regions of Japan [33].
- **Improving controllability and stability of a DC network** - By Equal Area Criterion, the generators go out of stability if the fault is not cleared within the critical clearing time; which is due to the excess kinetic energy stored in the rotor [9]. However, VSC HVDC has the capacity of reversing the power flow (by changing the current direction), so that it can quickly release energy to the healthy part of the system thus preventing the healthy part of the system from going into instability.

Furthermore, the ability to control the active and reactive power independently on an HVDC system has given a higher degree of freedom in power control. The flexibility is also due to the four-quadrant operation possibility in VSC mode [20].

- **Smaller environmental impact** - In a global effort to reduce greenhouse emissions, the power industry has been utilizing renewable energy sources to satisfy power demands. HVDC technology offers a solution to integrate these renewable energy sources into the electrical network.

Thus, providing a feasible alternative to fossil fuel-based energy sources. Furthermore, since the usage of HVDC technology results in lower power losses in comparison to AC transmission technology, lesser energy is wasted. The implementation of HVDC systems also uses less land and fewer transmission lines when compared to AC systems [13].

- **Cost** - Figure 1.1 depicts a plot illustrating the relationship between cost and distance for both HVDC and HVAC transmission systems. For shorter distances, HVAC transmission systems are economically viable, but for longer distances, they become more costly. Conversely, HVDC transmission systems are ideal for efficiently transmitting large amounts of power over extended distances. This disparity is attributed to the differing costs of transmission lines and terminal equipment. The distance after which employing HVDC transmission becomes more cost-effective than HVAC transmission is known as the break-even distance, which is approximately 80km [48].

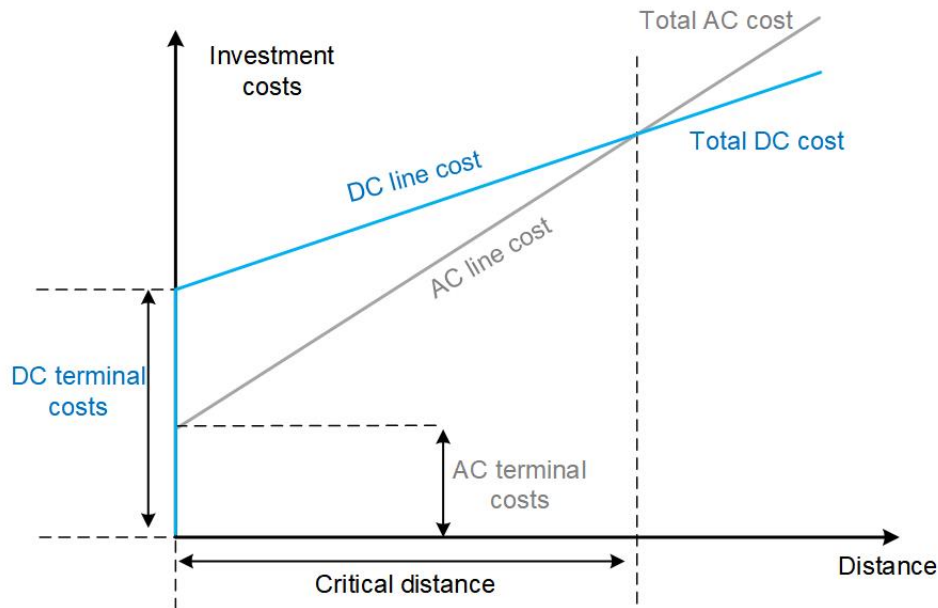


Figure 1.1: Cost comparison of HVAC and HVDC transmission. [1]

1.3. Motivation

The unpredictability of DC faults in electrical systems presents significant challenges in detecting and mitigating them. These faults, arising from insulation failure, lightning strikes, or short circuits, can emerge anywhere in the transmission system, causing current surges and DC voltage drops. DC faults in HVDC systems can lead to uncontrollable current flow in diode bridges during self-protection, particularly in converters using GTOs or IGBTs [6].

In the context of a two-level converter configuration, as shown in Figure 1.2, DC faults expose anti-parallel diodes, enabling fault current to flow through both AC and DC sides. Due to the diodes' minimal resistance, the discharged current from AC to DC rises, reaching unsustainable levels that can damage the diodes. This situation creates a series of problems, which include rendering power transmission impossible, potentially causing AC system collapse, and subjecting diodes to high short-circuit currents.

Even though an AC circuit breaker can clear the fault with a fault clearing time of 10ms or more, the power electronic devices cannot survive for this duration [16]. The rapid detection and clearance of faults are critical to prevent damage and ensure uninterrupted power supply. Moreover, high-frequency transient components generated during DC faults can destabilize the system, highlighting the importance of quick fault response.

The foundation of HVDC protection strategies draws upon established principles from HVAC protection methodologies. Within the scope of Multi-Terminal DC (MTDC) protection, three fundamental protection philosophies are employed: fully selective, non-selective, and partially selective. Under the fully selective approach, individual lines are shielded using high-power DC circuit breakers (DCCBs)

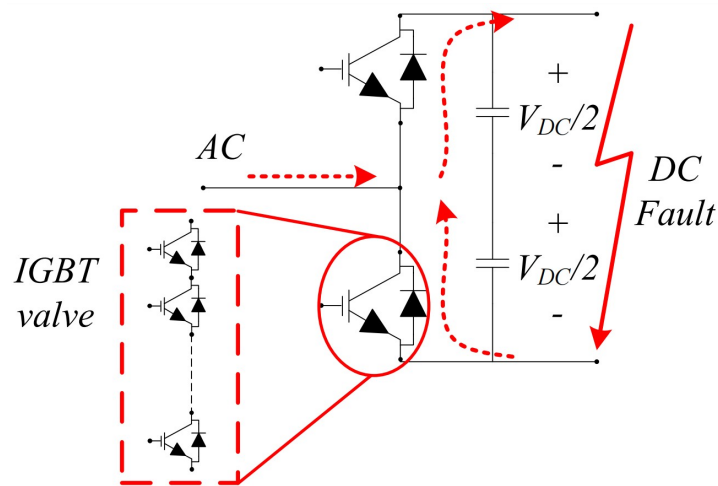


Figure 1.2: The fault current path of an IGBT-based two-level converter during a fault (for one phase) [59]

at both terminal points, ensuring continuous power flow across the grid. The protection schemes under the fully selective approach can be classified into communication-based (Unit) protection and local measurement-based (Non-Unit) protection. Examples of each category have been presented in Figure 1.3, along with the categories of protection philosophies. The non-selective philosophy treats the entire HVDC grid as a unified zone, relying on converters equipped with fault-blocking capabilities or alternating current circuit breakers (ACCBs) for protection, while in fully selective strategies, only the faulted segment is tripped without affecting the remaining healthy grid via installing DCCBs at both ends of each segment. Striking a balance between the two, the partially selective philosophy categorizes the grid into multiple protection zones, guided by the positioning of DCCBs, converters with fault-blocking capabilities, and ACCBs.

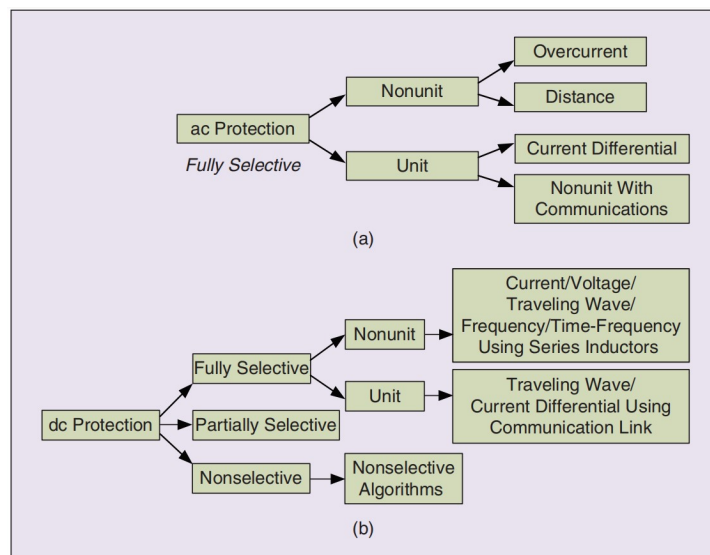


Figure 1.3: Categories of protection philosophies) [32]

Thus a fast, reliable, sensitive, and selective fault protection algorithm is required to accurately identify the DC line faults within a protection zone. It is crucial that the fault detection algorithm is able to detect various kinds of faults such as the positive Pole-to-Ground (PTG), negative pole-to-ground (NTG), and Pole-to-Pole (PTP) faults with different fault resistances. Furthermore, the algorithm should have the ability to differentiate a fault occurring outside the line (external fault) from a line fault (internal fault).

Research in the fields of DCCB and AC/DC converter design also contributes to making the HVDC system more robust and fault-resilient. In particular, the AC/DC converters play a significant role in operating the power systems: they control power flow, balance DC voltage, and can support an AC grid or even passive loads. Thus, improving their defense against DC faults is necessary to ensure the power system's availability. Unlike the AC system, the DC current and voltage have no zero-crossing points essential to interrupt the fault. Therefore, DCCBs must create a zero-crossing point to establish a robust HVDC network, and the acting time of DCCB has to be fast.

1.4. Research Questions

The key research question posed in this thesis is "How to protect an HVDC system in a reliable and selective manner?" The answers sought in response to this question are intended to establish a protection mechanism that can consistently operate when a fault condition arises (robustness) while ensuring the isolation of only the faulty section within the power system (selective). This means that any unnecessary or false protective actions should be minimized or avoided.

It's worth noting that while the design of AC/DC converters and DCCBs holds significant importance in HVDC protection, the scope of this thesis is limited to the domain of protection algorithms. The principal dedication of this research lies in the comprehensive analysis of such existing protection schemes. Thus, the central research question has been divided into two sub-questions -

1.4.1. HOW CAN DC FAULTS BE DETECTED IN A FAST AND ACCURATE WAY?

Effective fault detection in current or voltage forms the prerequisite for initiating subsequent protective actions, such as relay commands and the activation of DCCBs to interrupt fault currents. Precision in fault detection is paramount since incorrect tripping could lead to an unnecessary disruption of the power supply. Conversely, failure to promptly detect a DC fault due to algorithmic shortcomings could have catastrophic consequences.

Furthermore, given the inherent delays introduced during the protection process—ranging from the algorithm's execution time to signal transmission through channels and DCCB response time—swift action is imperative. In the event of a fault-generated wave, the protection system must identify it and command the DCCB within a tight 2ms window [30]. Consequently, the fault-detection algorithm must be capable of processing transient signals within this timeframe, without triggering a false tripping event. Therefore, it is important to answer the question: How can DC faults in an HVDC transmission line be detected in a speedy and accurate way?

1.4.2. HOW CAN THE PROTECTION'S SELECTIVITY BE ENSURED?

Selectivity holds a significant role in protection schemes, signifying that the faults inside the DC line (internal faults) are distinguished from faults outside the DC line (external faults). Hence, it is important to research the question: How can DC faults in an HVDC transmission line be detected with minimal false alarms?

1.5. Research Objectives

The purpose of this thesis is to perform a comprehensive analysis of the trade-offs among key performance attributes in four protection algorithms. The investigation delves into the interplay between selectivity, sensitivity, robustness, and speed, aiming to understand how these factors interact and influence the algorithms' overall effectiveness in HVDC system protection. By systematically examining the relationships and trade-offs among these attributes, this study seeks to provide valuable insights into the nuanced decision-making process involved in selecting an optimal protection algorithm.

- **Implementing protection algorithms in PSCAD, and MATLAB** - The research methodology involves the implementation and thorough testing of four distinct HVDC protection algorithms on a simulated HVDC system model using the PSCAD/EMTDC software platform. The HVDC model used is the 4 terminal model from the CIGRE B4.57 working group. All four protection algorithms have been implemented in the PSCAD environment. The performance of each algorithm in the presence of noise was tested in MATLAB. With the algorithms in place, comprehensive testing scenarios are designed to replicate various fault conditions that the HVDC system might

encounter. These scenarios encompass PTG faults, NTG faults, PTP faults, and various external faults to assess the algorithms' ability to accurately detect and selectively isolate faults.

- **Investigate how various fault parameters affect the performance of each algorithm** - The investigation entails a comprehensive exploration into the impact of diverse fault parameters on the efficacy of each protection algorithm. These fault parameters encompass fault resistance, fault location, and fault type, all of which play pivotal roles in influencing fault detection outcomes within the algorithms. For a set fault type and fault distance, the fault resistance is varied to analyze how it affects the protection algorithms. Similarly, the fault distance is varied, while keeping the fault resistance fixed for a set fault type.

This is repeated for different fault distances and different fault types. Through this systematic investigation, a comprehensive understanding of how fault parameters interact with the protection algorithms is established. The outcomes will provide insights into the algorithms' robustness against diverse fault conditions.

- **Determination of the optimal threshold values for each algorithm** - The threshold values serve as crucial parameters within these algorithms, as they dictate the point at which a transient signal is deemed indicative of a fault condition. Setting these values optimally is a delicate balance – too low, and the algorithms might be prone to false positives, needlessly triggering protective actions even during minor disturbances.

However, if the set threshold values are too high, there's a risk of failing to detect actual fault events. By subjecting the algorithms to different fault scenarios with incremental changes in threshold values, the thresholds that accurately capture genuine fault signals without triggering false alarms are identified.

- **Analyze the performance of the protection algorithms in terms of selectivity, sensitivity, robustness, and speed** - The selectivity of the algorithm, the ability to precisely identify and isolate the faulted segment has been analysed in this study by simulating various external faults and monitoring the response of the protection algorithm.

Sensitivity, the algorithms' responsiveness to genuine fault signals, has been analyzed in this thesis by subjecting each protection algorithm to different fault types and fault conditions. The performance of each algorithm is monitored in each case and then analyzed.

Robustness, reflecting the consistency of an algorithm's performance across varying conditions, is another dimension of analysis. Algorithms that demonstrate consistent fault detection and protective actions exhibit high robustness. The study aims to test the algorithms' robustness against noise.

Speed, the promptness with which an algorithm detects and responds to a fault, is essential for preventing damage to power electronic devices. To this extent, the trip time of each algorithm for each fault case was monitored and analyzed.

By systematically assessing the performance of the algorithms, the study seeks to provide a comprehensive understanding of how the algorithms' performances are influenced by design choices and parameter settings, aligning with the overall objective of enhancing protection strategies.

1.6. Outline of Thesis

The structure of the thesis is outlined as follows:

- **Chapter 2:** Introduces the concept and necessity of HVDC protection along with a comprehensive literature review of existing state-of-the-art HVDC protection schemes. Different fault types and their causes have been outlined in this chapter followed by a comprehensive review of various unit and non-unit protection algorithms that have been implemented in the past.

- **Chapter 3:** Introduces the 4 HVDC protection algorithms that will be studied in this thesis. The algorithms discussed are based on - Current differential deviation, ROCOV, ROCOC, and DC Reactor Voltage Change Rate. The theory behind each algorithm is explained along with its operation. For each algorithm, a flow chart summarizing the steps involved is presented.
- **Chapter 4:** Introduces the test system modeled in PSCAD for fault simulation and data extraction. Firstly, the schematic of the test system is presented. Furthermore, the function of each component of the HVDC system model is described. Lastly, the PSCAD model parameters for components such as generators, the load, and transformers have been provided.
- **Chapter 5:** Studies the fault cases on each protection algorithm with different fault resistances, fault distances, and fault types. The simulation results from PSCAD are monitored and reported for different fault cases. Furthermore, the algorithm's robustness against noise is evaluated. The threshold determination criteria for each algorithm have been discussed in this chapter as well. Lastly, the effect of varying the sampling frequency on the performance of each algorithm was monitored.
- **Chapter 6:** Summarizes, and compares the results of the performance of the algorithms presented in Chapter 5 in terms of their speed, sensitivity, selectivity, and robustness. The effect of the fault parameters and the influence of noise on each algorithm's performance has been discussed in this chapter.

2

A VSC-HVDC Grid Based Test System

2.1. Introduction

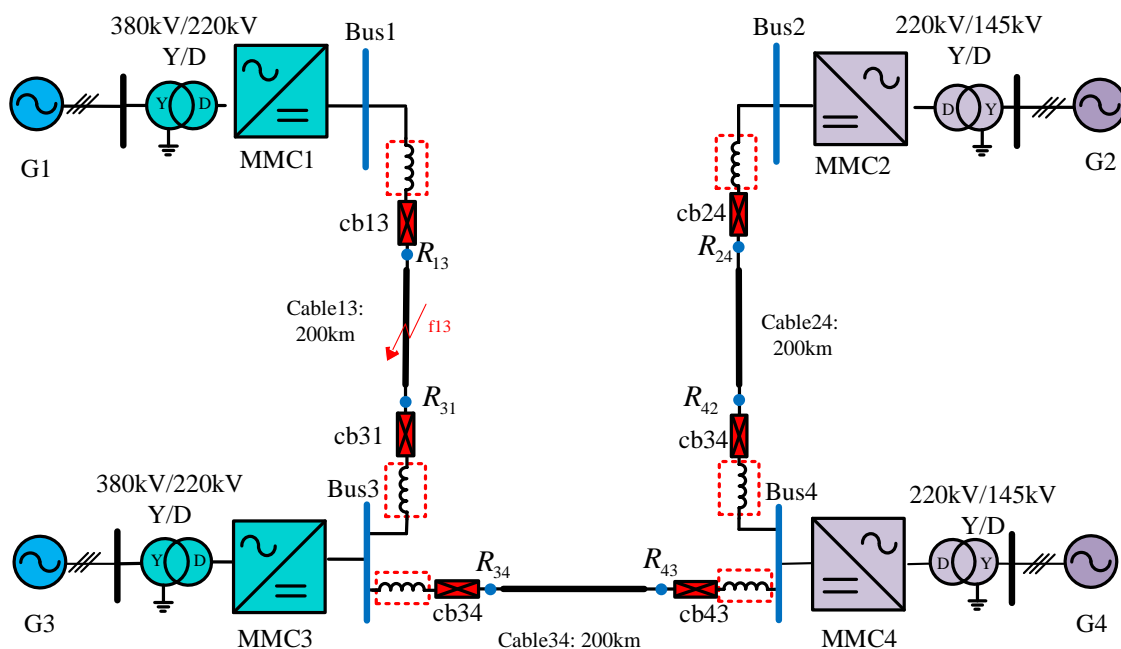


Figure 2.1: Test DC System

The test system employed to analyze the protection algorithms in this thesis is a four-terminal system based on the CIGRE B4.57 working group implemented in the simulation platform 'PSCAD/EMTDC'. The schematic of the test model is shown in Figure 2.1. This configuration forms a meshed VSC-HVDC Grid-Based test system. Each bus in the test system is connected to a local generator through an MMC and an external three-phase transformer. The three-phase transformers are used to convert the primary voltage level of the generators to a unified voltage level of 220kV AC, which is then converted to a voltage level of ± 200 kV DC through the MMCs. The primary voltage levels for the generators G1, G2, G3, and G4 are 380kV, 145kV, 380kV, and 145kV respectively.

Each MMC is equipped with its own dedicated control strategy, enabling them to fulfill their specific roles within the system. MMC1 and MMC3 operate in PVQ control mode while MMC2 and MMC4 operate in the islanded mode and PQ control mode respectively. All branches (Cable13, Cable34, Cable24) have a length of 200km. Furthermore, current limiting inductors are placed at each end of every branch to prevent the fault current from rising too quickly. Fault f13 represents the different types of internal faults triggered on Cable13 for the purpose of testing various protection algorithms.

2.2. MMC

The MMC is utilized to transfer a substantial amount of electrical power between AC and DC systems. The MMC consists of sub-modules (SMs) with two main topologies: the full-bridge (FB) structure and the half-bridge (HB) structure. The CIGRE model used in this thesis consists only of HB SMs, as depicted in Figure 2.2.

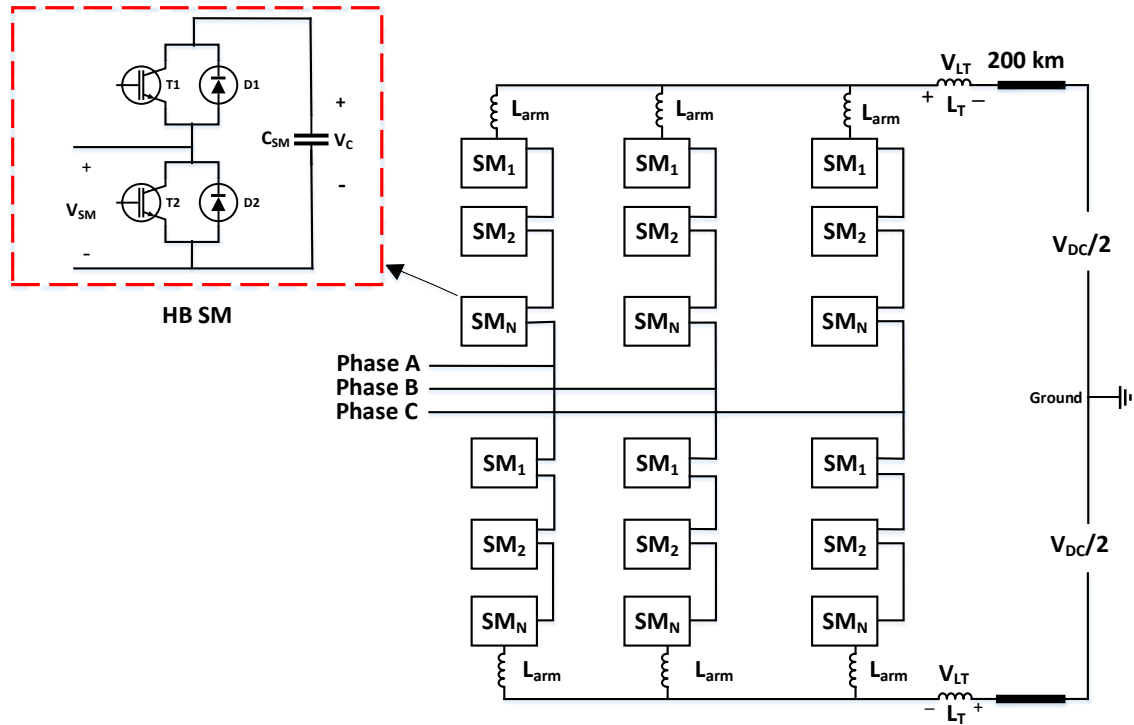


Figure 2.2: MMC Structure [24]

In Figure 2.2, three arms are connected to three separate phases: Phase A, Phase B, and Phase C. Each arm is composed of multiple HB SMs connected in series. The voltage at the midpoint of each phase leg is determined by the number of SMs connected in the upper and lower arms of the converter. When encountering a DC fault, both IGBTs T1 and T2 are switched off, but the fault current continues flowing through the antiparallel diodes in each HB SM. Under such a condition, the conducting HB SM effectively outputs zero voltage. High fault currents are fed by the AC grid due to the low impedance in the fault current path until the MMC is either isolated from the fault on the DC side via DCCBs or disconnected from the AC grid by ACCBs [24].

2.3. Terminal Inductors

Inductors positioned at the terminals of cables play a significant and indispensable role in safeguarding DC systems, functioning as current limiters. The main specifications of these terminal inductors are to have zero impedance during normal operation, and high impedance during fault conditions. These inductors serve two primary purposes. First and foremost, their presence acts as a preventive measure, preventing the rapid escalation of DC fault currents. These inductors can be classified as self-controlled, externally controlled, and hybrid-controlled. The self-controlled current limiting inductors have a simple structure with high-speed response, while externally controlled types have high accuracy and certainty of operation. The hybrid-controlled current limiting inductors benefit from the advantages of both topologies [8].

Secondly, the inclusion of these inductors introduces variability in the magnitude of current surges

and voltage drops experienced by the inductors during a fault. This variation serves as a valuable detection criterion, the sharp increase in the inductor voltage during a fault in particular is used to establish a fault detection criterion in one of the protection algorithms evaluated in this thesis [25]. In the test model used in this thesis, the inductance of the terminal inductors has been set to 40 mH. To evaluate the effect of inductance on the performance of the protection algorithms, the inductance of the terminal inductors has been varied from 10mH to 80mH.

3

State-of-the-Art HVDC Protection Algorithms

3.1. Introduction

HVDC protection algorithms lie at the core of a fault-clearing mechanism. They are designed to detect faults in HVDC transmission systems to prevent damage to the equipment and ensure reliable operation. This is achieved by sending the trip signal, based on the outcome of the protection algorithm, to the relay units associated with the appropriate circuit breakers. The circuit breakers then isolate the faulty line from the rest of the network.

These algorithms can be broadly classified based on their intended protection function and speed as primary and backup protection algorithms. Primary protection algorithms are designed to detect and clear faults quickly to prevent damage to the HVDC transmission system. These algorithms are typically fast-acting and are activated automatically in response to a fault. Backup protection algorithms are intended to provide secondary protection in the event of a failure of the primary protection algorithm. These algorithms are typically slower-acting than primary protection algorithms and are activated only if the primary protection algorithm fails to operate.

Another way to classify HVDC protection algorithms is based on their need for a communication channel. Non-unit protection algorithms do not require a communication channel and operate independently at each end of the transmission line. These algorithms are also known as communication-less or non-pilot algorithms. In contrast, unit protection algorithms require a communication channel between the two ends of the transmission line to exchange information and coordinate protection actions. These algorithms are also known as communication-based or pilot algorithms.

3.2. Unit Protection Algorithms

Unit protection systems use a communication channel to exchange signals between the relays located at each protection zone end. These communication-based algorithms offer inherent selectivity but depend on a swift and reliable communication medium. The communication media can be metallic wires (electric signals), air and space (microwaves or radio), or optical fibers (light signals). In the context of HVDC grids, satellite communication is unsuitable due to the significant travel time involved. Consequently, optical fiber emerges as the optimal transmission medium due to its rapid transmission speed. However, even with optical fiber, there exists a signal propagation delay on lengthy cables. The signal propagation delay time experienced on a 100-kilometer-long cable made of fiber optic is assumed to be around 0.5 milliseconds. This delay becomes noteworthy when considering the swift rise of DC current during fault scenarios. Consequently, fiber optic communication systems might struggle to fulfill the speed requirements for promptly detecting and resolving faults, particularly over substantial distances. Furthermore, deploying a high-speed communication system incurs significant costs. Due to these challenges, a unit protection algorithm should only be applied in HVDC protection systems to enhance and/or optimize their performance. Such an algorithm can serve as a backup protection mechanism or be employed in scenarios involving high-impedance faults where such a fast operation

is not needed [3]. Unit protection algorithms can be further classified into differential protection and directional protection.

3.2.1. Current Differential Protection:

Current differential protection is a prevalent method employed for safeguarding various units such as bus bars, converter stations, and DC lines. This technique involves the utilization of relays placed at both ends of the protected unit, with each relay monitoring the local current and transmitting this data to the opposite end. Consequently, both relays possess current information from both extremities, enabling them to juxtapose these values and ascertain any discrepancies against a predetermined threshold. This assessment yields a "differential current," which, when surpassing a preset threshold, indicates the presence of a fault.

In [11], the line-mode backward traveling wave (TW) is utilized to establish differential protection. The operational principle revolves around employing the differential of the backward-TW between the two relevant terminals. Another algorithm uses fault-tolerant inductor-capacitor-inductor VSCs with mechanical DCCBs to limit fault currents and achieve highly selective protection based on a current differential criterion [12]. The algorithm in [7] uses the Bergeron model to achieve differential protection.

Although current differential protection offers notable advantages such as robustness, precise selectivity, and clear directionality, it is not devoid of shortcomings. One significant drawback stems from the reliance on signals from both terminals, necessitating the establishment of a communication link. This communication requirement introduces reliability demands, introduces time delays, and synchronization complexities. Consequently, each relay must factor in and compensate for communication-induced time delays to accurately retrieve the relevant current value. This challenge is further compounded by the necessity for precise timestamped data from both ends.

The drawbacks are particularly pronounced in scenarios involving longer DC lines within the HVDC grid. Longer lines entail extended communication time delays, rendering the application of current differential protection less feasible. This issue is even more pronounced when faults occur near one of the terminals, as the time delay becomes more significant. Nonetheless, for systems with shorter DC lines, current differential protection remains a viable choice.

Furthermore, current differential protection is well-suited for securing bus bars, where discrepancies between incoming and outgoing currents are measured. Should such discrepancies be non-zero, the method promptly detects faults occurring within the substation. Despite its challenges, current differential protection remains a dependable choice for numerous scenarios, albeit with careful consideration of its limitations and suitability to specific system configurations [43].

3.2.2. Directional Protection:

Directional protection constitutes another communication-based approach. In this method, each relay shares solely the direction of the current with the opposing end when a fault is detected. Should the relays at the protected line's extremities identify a fault in their respective forward directions, a trip command is initiated, leading to the isolation of the line. The strength of this method lies in its simplicity, as it transmits minimalistic information (the sign of the current). This simplicity contributes to heightened robustness compared to the current differential method. Nevertheless, like other communication-dependent protection strategies, directional protection grapples with challenges stemming from communication-induced time delays and transmission-related issues.

[64] uses the Wavelet Transform Modulus Maximum (WTMM) technique to determine the orientations of transient fault currents at line ends and compare them to identify internal and external faults. The algorithm proposed in [26] compares the orientations of transient energies (TEs) computed from the initial fault voltage TWs at both cable ends. [34] proposes a directional algorithm based on the integral of reactive power for HVDC systems. The directional characteristics of reactive power flow are theoretically analyzed for internal and external faults, and these characteristics are used to construct the protection algorithm. The Hilbert transform is adopted to calculate the reactive power, which ensures a continuous output of calculation results and improves the reliability of the protection.

While offering an effective means of discerning fault direction and reacting promptly, directional protection is not exempt from the broader communication-associated limitations. These encompass the necessity for reliable communication links, potential delays in data transmission, and synchronization intricacies. Despite these drawbacks, the directional protection technique presents a more straightforward alternative to current differential protection, with its resilience further underscoring its suitability

for certain scenarios [43].

3.3. Non-Unit Protection Algorithms

Non-unit protection algorithms differ fundamentally from their unit-based counterparts by functioning independently of communication channels. This eliminates the requirement for communication mediums, thus also avoiding the inherent communication delays. Their integration into HVDC protection systems holds the potential to amplify protection performance. In a non-unit protection system, the reliance is solely on local data collected from each terminal. This typically involves utilizing these quantities along with derived mathematical variables to identify faults. These quantities are the DC currents, DC current derivatives, DC voltages, and DC voltage derivatives [40]. Discussed below are some of the state-of-the-art non-unit protection algorithms in the industry. The advantages and disadvantages of each type of non-unit protection algorithm have been summarized in Table 3.1

3.3.1. Overcurrent and Undervoltage-Based Algorithms -

Overcurrent protection represents a straightforward approach to detecting faults in electrical systems. This technique involves monitoring current levels at a single terminal. This approach is prominently utilized in the protective philosophy of IGBTs within VSCs. The fundamental concept entails setting a threshold current value, and if this value is surpassed, a fault is identified. The inherent DC voltage ensures current directionality is discerned by simply observing current polarity. The overcurrent principle is applied in [56], where an inverse time overcurrent algorithm is proposed for the protection of MTDC grids. Another simple overcurrent algorithm is realized in [2].

Faults can also be detected by the observed diminished voltages. In this regard, under-voltage relays can serve as indicators of fault occurrences. Analogous to overcurrent detection, an under-voltage methodology entails setting a voltage threshold. If the measured voltage drops beneath this threshold, a fault is identified. The under-voltage technique can also serve as supplementary protection or be incorporated as one of the criteria for fault detection within a holistic protective design [43]. The under-voltage criterion has been used as a startup condition to trigger the protection algorithms described in [21]. In [22], it is implemented as a backup protection algorithm.

The advantage of the overcurrent and undervoltage-based algorithms is that they are very simple in theory as well as in implementation. However, while the undervoltage-based algorithms are faster than current-based ones due to the sharp voltage drop, both algorithms suffer from slow operation speeds. Furthermore, these algorithms have poor selectivity.

3.3.2. Current and Voltage Derivative-Based Algorithms -

The rate of change of voltage or current signals, namely dv/dt and di/dt are useful criteria for designing DC fault analysis methods. Analogous to the under-voltage method, these methods utilize the rate of change of voltages (ROCOV). This method has the advantage of being very fast because it is based on the first incident wave, which allows for quick detection. Likewise, analogous to the overcurrent method, the rate of change of current (ROCOC) in the DC line is the fault-deciding criterion.

One proposed algorithm [50] utilizes local terminal inductor voltage measurements to estimate the ROCOV value, which is then compared to a pre-adjusted threshold for DC fault detection and localization. Another fault detection system using ROCOV measured locally at the line side of the inductors is proposed in [51]. Another ROCOV-based algorithm is proposed in [41].

In [14], five ROCOC indices are computed to detect various faults (including those involving the metallic return conductor in asymmetric bipolar setups) and to identify the faulty pole. The protection algorithm described in [37], sets a threshold on the current derivative to detect a line fault in the HVDC system. This acts as the primary protection algorithm that copes with low-impedance faults. Furthermore, a fault detection method based on identifying suited fault detection variables or markers, i.e. DC current and voltages derivatives and locally measured magnitudes is proposed in [36].

The voltage and current derivative-based methods offer better speed and selectivity than the overcurrent and undervoltage-based algorithms. Furthermore, they are simple to implement and can operate on a low sampling frequency. However, it fails to detect faults having a high fault resistance. These faults are known as High impedance faults (HIFs). Furthermore, the derivative-based schemes are vulnerable to maloperation due to noise.

3.3.3. Terminal Inductor-Based Algorithms -

Under normal operation, the voltages across the terminal reactors are assumed to be negligible or close to zero. However, in the event of a DC fault, a swift decrease in the line voltage is observed, resulting in high DC voltages across the terminal reactors. This rise in terminal reactor voltage can be thus used as a fault-detection criterion in HVDC systems. A method based on the rate of change of inductor voltage is discussed in [25]. The concept of asymmetric pole inductors has been proposed in the protection algorithm introduced in [4], where the difference between the inductor voltages of the two poles is utilized as the fault detection criterion. The algorithm proposed in [23] compares the inductor voltages between negative and positive poles to identify faults. The algorithm proposed in [60] uses modal analysis where the line-mode inductor voltage is adopted for fault identification, while the zero-mode inductor voltage is adopted for faulted pole selection.

Protection algorithms based on the terminal reactor have the advantages of simple implementation, low computation, and noise resilience. Furthermore, due to the reactor voltage being directly proportional to the second derivative of the DC line current, protection algorithms based on the reactor voltage are more robust than the overcurrent and ROCOC-based algorithms. However, the algorithms based on the terminal inductor fail to distinguish HIFs from external faults.

3.3.4. Time-Domain TW-Based Algorithms -

In the event of a DC fault on the transmission line, transients of high-frequency voltage and current waves are generated which tend to circulate between the line terminals and the fault point. These transients are known as TWs.

The protection algorithms utilizing this concept are based on the time difference between the first arrived TW from the fault and the first reflection from the fault measured at the local terminal.

For instance, the method proposed in [61] uses current measurements for the first ms of the transient period of the DC fault to obtain a time-domain fitting of the fault current. The fitting coefficients are used as an indicator for discriminating between external and internal faults. The proposed method in [55] utilizes current and voltage measurements to derive the difference between the surge arrival time of the zero-mode and line-mode TWs.

Although these methods offer fast detection speeds and are easy to implement, they heavily rely on TW amplitudes, which impose low sensitivity under HIFs and are susceptible to noise. Furthermore, TW-based methods require a large sampling frequency.

3.3.5. Frequency Domain-Based Algorithms

During a fault, the TW arrives from the fault to the local terminal. Part of the wave is reflected from the local terminal and travels back to the fault, followed by a reflection from the fault location. Due to these multiple reflections, the transient voltage possesses plentiful high-frequency components. As a boundary element, the current-limiting inductors smooth the wave heads of the TWs and attenuate their high-frequency components. Therefore, the amplitudes of the change rate of DC line voltage and the high-frequency components in transient voltage are much larger under internal faults than those under external faults [57].

These high-frequency components can thus be employed to develop non-unit HVDC protection algorithms. Different mathematical tools have been proposed to extract these components such as the Fourier Transform (FT), the Wavelet transform (WT), the Hilbert-Huang Transform (HHT) and the Stockwell transform (ST). The following section describes a few state-of-the-art protection algorithms based on each tool.

- **Fourier Transform** :In [17], the authors present an innovative algorithm for locating faults in MTDC systems. This algorithm utilizes natural frequency and relies solely on current measurements. The process involves identifying frequency spectra for each terminal using the fast Fourier transform (FFT) and calculating the dominant frequency component. In [63], the First Carrier Frequency Harmonic currents, which are extracted using the discrete Fourier transform (DFT), are employed as the key feature to detect and identify fault conditions in transmission systems equipped with PWM converters. [47] utilizes the FFT to extract the high-frequency components from the line-mode current TW to identify and locate faults in the HVDC line.

The FT-based protection algorithms are the simplest and the least computationally intensive among the frequency-based methods on WT, HHT, and ST. Despite their fast processing speed,

the FT-based algorithms suffer from poor time-frequency resolution and cannot provide any information in the time domain.

- **Wavelet Transform** :In [54], the wavelet transform is used to extract the high-frequency components from the DC voltage signal, and an Artificial Neural Network (ANN) is used to identify the fault type. The protection algorithm proposed in [42] follows a two-stage approach. The first stage is a parameterization procedure to select the optimum WT parameters (which is carried out offline) and the second stage is a real-time signal processing process that is responsible for extracting the high-frequency components in the voltage TW and consequently, for detecting internal faults. The WT-based algorithms described in [38] and [46] utilize the wavelet transform coefficients calculated for the voltage and current TW respectively for fault detection. In [27], the energy content associated with both the low and high-frequency components of the transient voltage TW is extracted to determine a fault-case scenario. In [31], the Stationary wavelet transform (SWT) is adopted to process the rectifier side DC voltage, and then wavelet modulus maxima are used to develop a novel non-unit HVDC protection algorithm.

WT-based algorithms offer exceptional filtering ability, enabling precise signal decomposition into distinct frequency components and noise resilience. The WT-based algorithms also offer a higher time-frequency resolution than the FT-based algorithms, as they can provide information about the fault signal in the time as well as the frequency domain. However, the algorithms based on the WT are computationally intensive, require a high sampling frequency, and are complex to implement.

- **Hilbert-Huang Transform** :In the algorithm proposed in [52], HHT is applied to the DC voltage waves to extract the transient frequency and transient amplitude of the DC voltage. A support vector machine (SVM) learns the mapping between the transient frequency and transient amplitude of the DC voltage and desired outputs, fault type, and fault location through a training process. In [62], the HHT is used to extract the energy of the high-frequency components present in the line mode voltage TW to develop a fault-detection algorithm. The authors in [44] introduce a novel approach for fault location in VSC-HVDC systems using a hybrid system that combines an adaptive neuro-fuzzy inference system (ANFIS) with the HHT. The HHT is applied to extract new features from current signals, and the ANFIS utilizes these features to estimate fault locations in transmission lines. In [18], an Improved Complementary Ensemble Empirical Mode Decomposition with Adaptive Noise (ICEEMDAN) is used to extract the highest frequency oscillations of the initial fault voltage. Afterward, the high-frequency energy of the initial fault voltage is calculated by adopting the HHT, which forms the fault identification criterion.

HHT goes one step ahead of DWT and gives information in the time-instant frequency domain. The input signal is first decomposed into different components by using EMD, which are termed intrinsic mode functions (IMFs). HHT can adaptively decompose the signal into IMFs and also has enhanced time–frequency resolution when compared with WT. However, HHT-based algorithms also need high computation due to having complex mathematical operations and require a large sampling frequency.

- **Stockwell Transform** : In the protection algorithm proposed in [49, 53], the ST amplitude matrix is used to analyze the fault. Each row of the matrix displays the ST amplitude at the same time for all the frequencies and each column of the ST matrix presents the ST amplitude with time. In [45], the high-frequency components of the voltage and current waveforms from the power systems are analyzed by the ST and then the extracted features are fed as inputs to the classifier neural network to determine the fault conditions. An ST-based HIF detection algorithm is proposed in [28] which extracts the third harmonic current phase angle from the current TW, while the moving standard deviation continuously monitors this parameter. A fault is detected when the standard deviation is below a self-adaptive threshold for a predetermined period of time.

The ST utilizes a variable window size, where The window size becomes wider in the low-frequency band and shortens during the high-frequency band, thus providing a better time-frequency resolution than the FT-based algorithms. In addition, the computation of ST is relatively simple when compared to the calculation of WT, and HHT. However, it has poor time-resolution frequency when compared to HHT-based algorithms.

Protection principle	Advantages	Disadvantages
Overcurrent/Undervoltage ([56], [2], [21], [22])	Simple to implement	Slow, poor selectivity
Voltage/Current derivative ([50], [51], [41], [14], [37], [36])	Fast, simple to implement, low computation	Vulnerable to noise, poor selectivity against remote HIFs
Time domain TW ([61], [55])	Simple to implement	High sampling frequency, vulnerable to noise, slow operation speed for long DC lines
Terminal Inductor ([25], [4], [23], [60])	Simple implementation, low sampling frequency, noise resilient	Poor selectivity against HIFs
FT ([17], [63], [47])	Simple to implement can detect HIFs	Does not provide fault information in the time domain, for example, the time of fault inception
WT ([54], [42], [38], [46], [27], [31])	Fast, provides multi-resolution analysis (which provides localisation in time and frequency domains simultaneously), can filter out noise	High sampling frequency, complex implementation, computationally intensive
HTT ([52], [62], [44], [18])	Provides high-resolution analysis and can capture multiple intrinsic modes	Complex implementation, computationally intensive, high sampling frequency
ST ([49], [53], [45], [28])	Better time-frequency resolution than FT-based algorithms, computationally less intensive than WT	Poor time-frequency resolution compared to HHT

Table 3.1: Summary of non-unit HVDC protection algorithms

4

Examined Protection Algorithms

4.1. Introduction

The four HVDC protection algorithms that have been evaluated in this thesis are presented in this chapter. The underlying theory behind each algorithm's fault detection concept is discussed in detail, supported by relevant equations and circuit diagrams. The major processes in each algorithm are outlined in this chapter, which have been summarized in a flowchart.

The algorithms discussed are -

- DC fault detection using current differential deviation [39]
- DC fault detection using DC Reactor Voltage Change Rate [25]
- DC fault detection using ROCOV [50]
- DC fault detection using ROCOC [37]

4.2. Current Differential Deviation

In this thesis, for the purpose of data acquisition, currents at both terminals, R_{13} and R_{31} , of the positive pole and negative pole of Cable13 are measured and indicated by (I_{p13}, I_{p31}) and (I_{n13}, I_{n31}) respectively, as illustrated in Figure 4.1. The current limiting inductors in the protected line have been represented as 'L1', 'L2', 'L3', and 'L4'.

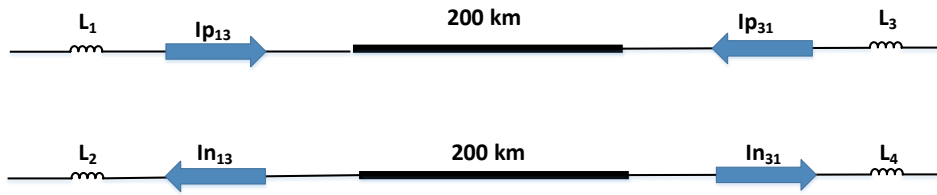


Figure 4.1: Data acquisition for current differential deviation-based protection

The current differential deviation for each pole is defined as the derivative of the current differential at that pole with respect to time. In order to trigger the protection algorithm, the recorded $\Delta \frac{dI_p}{dt}$ or $\Delta \frac{dI_n}{dt}$ must cross their respective thresholds $\Delta I_{p_{thresh}}$, and $\Delta I_{n_{thresh}}$ respectively. The current differential deviations in this thesis have been calculated as follows -

$$\Delta \frac{dI_p}{dt} = \frac{d(I_{p13} + I_{p31})}{dt} \quad (4.1)$$

$$\Delta \frac{dI_n}{dt} = \frac{d(I_{n13} + I_{n31})}{dt} \quad (4.2)$$

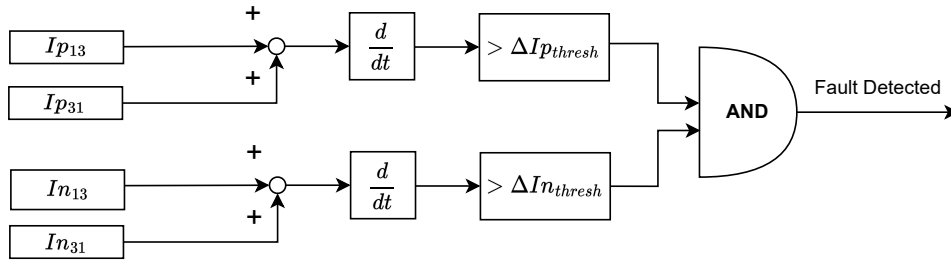


Figure 4.2: Logic scheme for current differential deviation-based protection

4.3. DC Reactor Voltage Change Rate

Under normal operating conditions, the converter generates the rated DC voltage v_{DC} . Moreover, the voltages across the upper and lower arm reactors (L_{arm}) and each of the two terminal reactors (L_T), as shown in Fig. 4.3, can be assumed to be zero:

$$v_u + v_l = v_{DC} = v_T = v_1 \quad (4.3)$$

$$v_{L_{arm}} = v_{L_T} = 0 \quad (4.4)$$

Where v_u , and v_l are the upper and lower arm voltages respectively. v_T is the MMC terminal voltage v_1 is the line side DC voltage v_{L_T} is the total voltage across the terminal inductor L_T

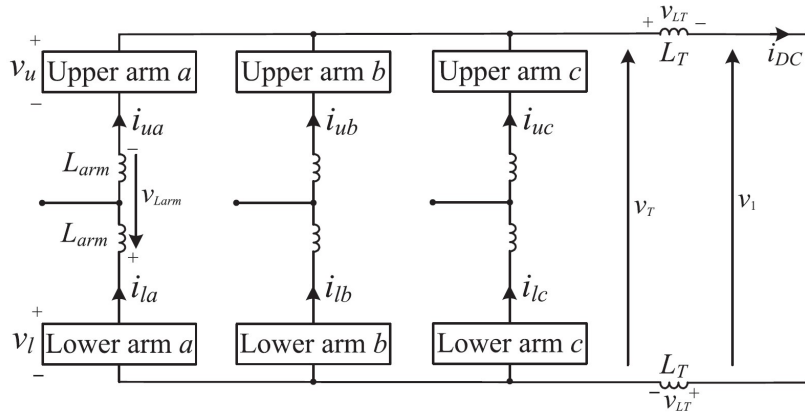


Figure 4.3: MMC with terminal inductors [25]

The DC fault results in a steep drop in v_1 . Additionally, high DC voltages arise on the arm inductors L_{arm} ($v_{L_{arm}} > 0$) and the terminal inductors L_T ($v_{L_T} > 0$). The voltage across the MMC at the terminal end, v_T , drops below the rated DC voltage, v_{DC} . Despite the occurrence of a DC fault, the converter continues generating and maintaining the specified voltage v_{DC} .

$$v_T = v_u + v_l - v_{L_{arm}} \quad (4.5)$$

$$v_u + v_l = v_{DC} \quad (4.6)$$

$$v_T \leq v_{DC} \quad (4.7)$$

Therefore, through careful analysis of the voltage across the terminal inductor, the presence of a fault can be promptly identified. The reactor voltage monitored in the protected line is depicted as v_{L_T} , as illustrated in Figure 4.3. Building upon this observation, a method is proposed for detecting and locating DC faults at the station by utilizing the voltage change across the terminal inductor. The equation forming the fault detection criteria is expressed in (4.8), where Δt represents the duration it takes for the voltage across the terminal inductor to increase from an initial threshold V_{L_T1} to the protection threshold V_{L_T2} .

$$\frac{V_{LT2} - V_{LT1}}{\Delta t} = \frac{\Delta v_{LT}}{\Delta t} = \frac{dv_{LT}}{dt} \quad (4.8)$$

By employing predefined thresholds V_{LT1} and V_{LT2} , the derivative of the terminal inductor voltage can be determined based on the time interval Δt . Monitoring this interval allows for faster detection, localization, and isolation of faults, resulting in reduced stress on converter components and circuit breakers caused by fault currents. The voltage across the terminal inductor is continuously measured, and only fault detections that are smaller than the threshold detection time, $t_{threshold}$ are considered valid. In other words, if the time interval Δt is shorter than $t_{threshold}$, the fault protection measures are activated.

The major processes involved in the algorithm are illustrated in Figure 4.4

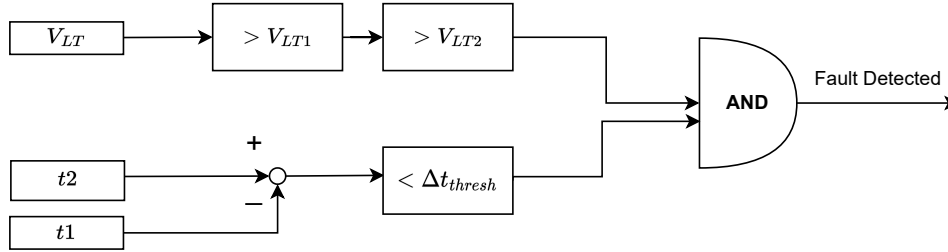


Figure 4.4: Inductor voltage-based algorithm flowchart

4.4. ROCOV

Consider the voltage measurement taken at the line side of breaker R_{31} for PTG faults, each fault case having a fault resistance of 100Ω , shown in Figure 4.6. These PTG faults are denoted as 'F1' in Figure 4.5. All faults are initiated at 1 s. Each plot corresponds to a different fault location on Cable13 (10, 100, 190 km from Bus 3). For the aforementioned faults, the slope (ROCOV) of the voltage wavefront is quite steep even up to 190 km down Cable13. The $|ROCOV|$ of the positive pole and negative pole, represented by $ROCOV_P$, and $ROCOV_N$ respectively, are calculated as follows -

$$ROCOV_P = \left| \frac{dV_{p31}}{dt} \right| \quad (4.9)$$

$$ROCOV_N = \left| \frac{dV_{n31}}{dt} \right| \quad (4.10)$$

Where, V_{p31} , and V_{n31} are the positive and negative pole voltages measured at R_{31} .

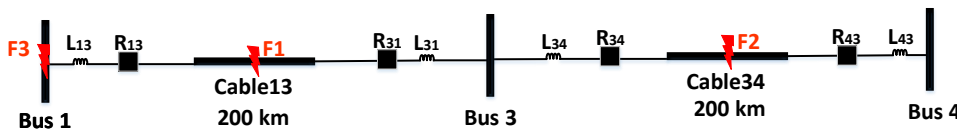


Figure 4.5: Simplified section of the 4 terminal CIGRE B4.57 model

In this algorithm, the absolute value of the ROCOV ($|ROCOV|$) is considered to form the protection. Figure 4.7 depicts the absolute value of $ROCOV_P$ depicted in Figure 4.6. The spike observed in $ROCOV_P$ during an internal fault is used to establish a threshold for the observed $|ROCOV|$ in the positive and negative poles.

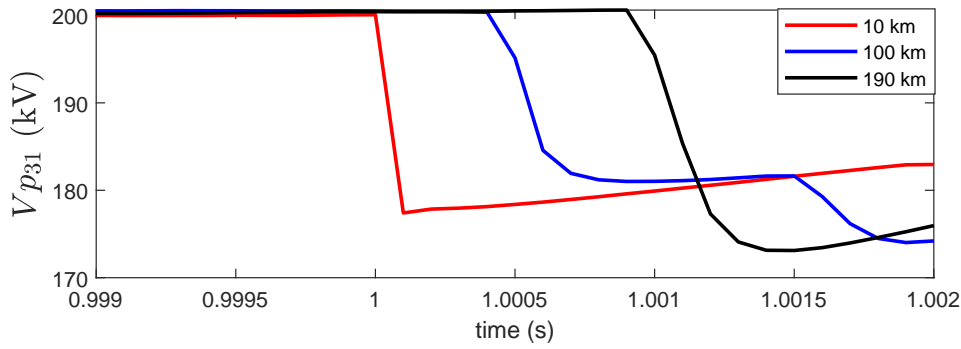


Figure 4.6: V_{p31} during internal faults

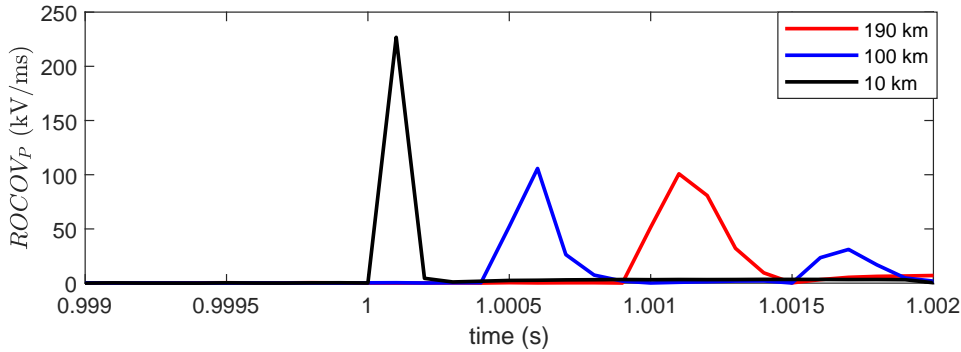


Figure 4.7: $ROCOV_P$ for internal faults

Figure 4.8 shows the line-side voltage measured at R_{31} for external faults F2, and F3. Fault F2 is a PTP fault ($R_f = 0 \Omega$, $x = 10 \text{ km}$) located 10 km from Bus 3, on Cable34. The last plot is voltage measured at R_{31} for external fault F3, a DC bus fault at Bus 1. This fault is separated from the fault at 200 km down the line by one current-limiting inductor.

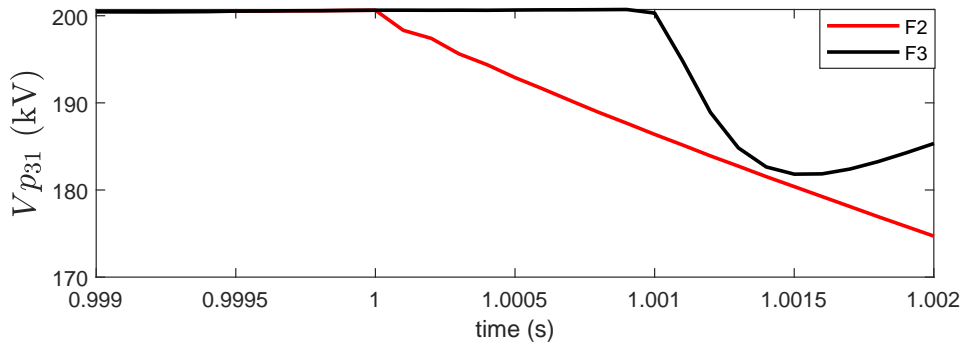


Figure 4.8: V_{p31} during external faults

As a result, the spike in $|ROCOV|$ is observed nearly 1 ms after the fault inception, as shown in Figure 4.9. Fault F2 is each separated from breaker R_{31} by two current limiting inductors. These inductors act as a low-pass filter and smooth out the voltage transient that is observed at R_{31} . As a result, a much more gradual voltage change as seen on the line side of R_{31} for fault F2, however due to the short distance between the fault location and R_{31} , the spike in $ROCOV_P$ is observed as soon as the fault is triggered.

Thus, the change in ROCOV (from almost zero steady state) can be used to detect the occurrence of a fault very quickly (within microseconds of the fault wave arriving at the current limiting inductor). The difference in ROCOV magnitudes can be used to differentiate internal faults from external faults. The measured $ROCOV_P$ and $ROCOV_N$ are then compared with the threshold value, denoted by $ROCOV_{thresh}$. If the recorded $ROCOV_P$ or the $ROCOV_N$ value crosses the threshold, the protec-

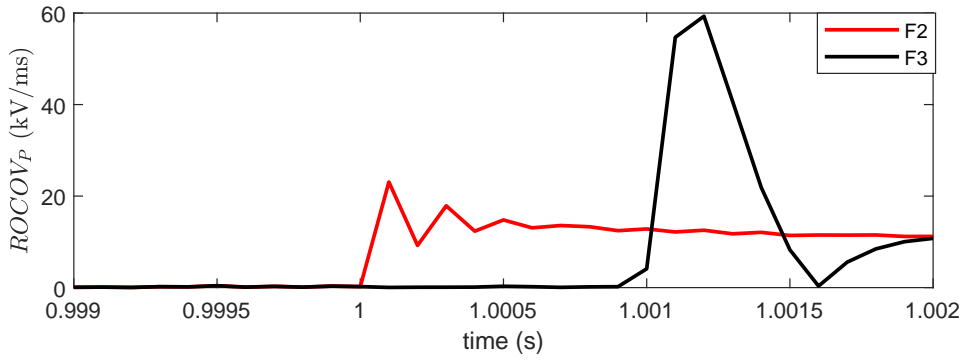


Figure 4.9: $ROCOV_P$ for external faults

tion is activated and the faulty branch is isolated. The processes involved in the algorithm have been summarized in Figure 4.10.

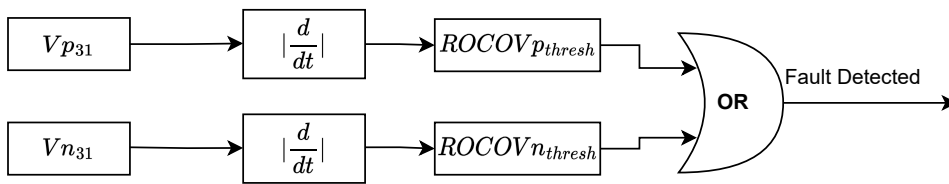


Figure 4.10: ROCOV-based algorithm flowchart

4.5. ROCOC

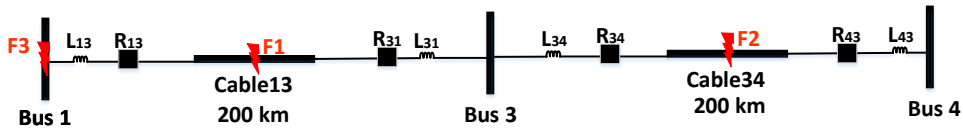


Figure 4.11: Simplified section of the 4 terminal CIGRE B4.57 model

The solution proposed in this paper utilizes the absolute value of the rate of change of the positive and negative pole currents, for detecting internal faults denoted by F1 in Cable13, as depicted in Figure 4.11. Figure 4.12 shows the data acquisition points for the ROCOC-based protection algorithm in the test system.

I_{p31} , and I_{n31} represent the positive and negative pole currents measured at R_{31} . Figure 4.12 shows the placement of the current measurement units at R_{31} . The $|ROCOC|$ of the positive pole and negative pole, represented by $ROCOCP$, and $ROCOCN$ respectively, are calculated as follows -

$$ROCOCP = \left| \frac{dI_{p31}}{dt} \right| \quad (4.11)$$

$$ROCOCN = \left| \frac{dI_{n31}}{dt} \right| \quad (4.12)$$

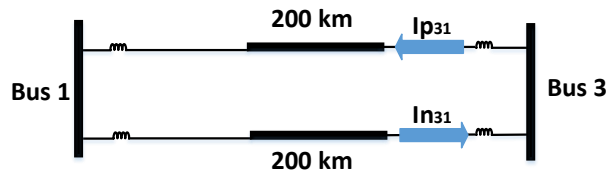


Figure 4.12: Current measurements for ROCOC-based protection

Figure 4.13 shows the measured positive pole current measured at R_{31} , I_{p31} in the event of a PTG fault, with a fault resistance of 0Ω . These internal faults are initiated at 1 second, and each plot corresponds to different fault locations on Cable13, which are 10, 100, and 190 kilometers from Bus 3. Even at distances as far as 190 km down Cable13, the steepness of the current waveform indicates that the ROCOC is a good indicator of the presence of a fault.

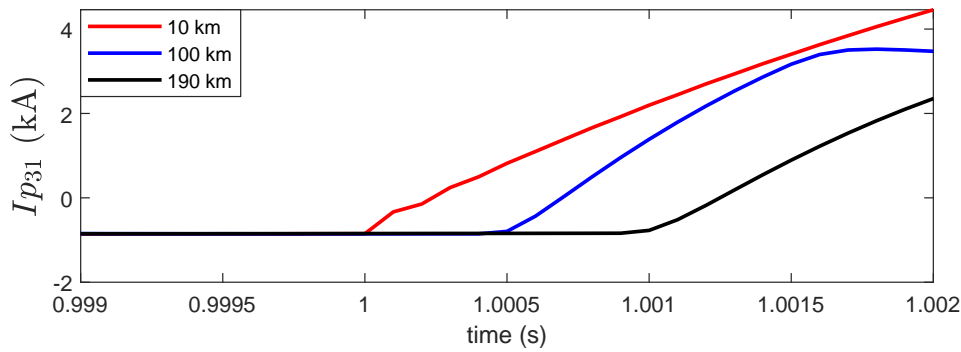


Figure 4.13: I_{p31} during internal faults

Figure 4.14 depicts the absolute value of the rate of change of positive pole DC current ($ROCOCP$) depicted in Figure 4.13. The sudden rise observed in $ROCOCP$ during an internal fault is used to establish a threshold for the observed $|ROCOCP|$ in the positive and negative poles.

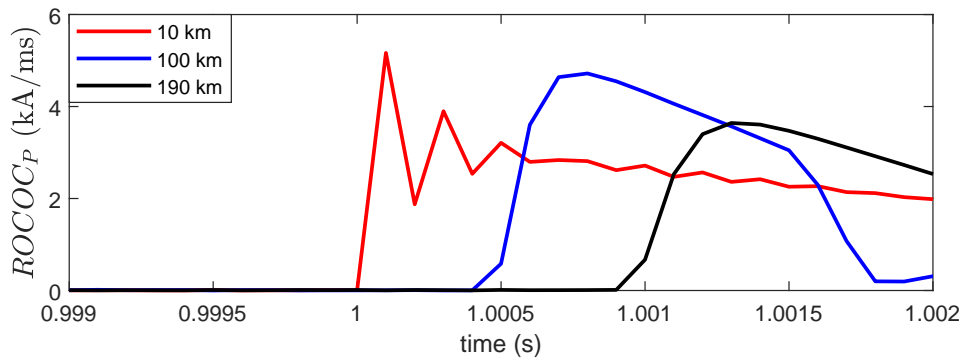


Figure 4.14: $ROCOCP$ during internal faults

Figure 4.15 presents the current measurements for a remote bus fault, fault F2 on Cable34, located 10 km from Bus 3, but this fault is separated from the breaker R_{31} by two current limiting inductors. Additionally, the paper discusses fault F3, which is a DC bus fault at Bus 1. This fault is situated at a considerable distance from the fault at 200 km down the line, and it is separated by one current-limiting inductor.

In these external fault scenarios, the current limiting inductors act as low-pass filters, which tend to smooth out the current transients. As a result, the current observed at R_{31} for faults F2 and F3 appears to exhibit a much more gradual change compared to the current for internal faults. This differentiation is due to the presence of inductors that attenuate the high-frequency components of the current waveform.

Thus, the slope of the fault current (ROCO) (from an almost zero steady state) can be utilized for the rapid detection of fault occurrences, often within microseconds of the fault wave reaching the

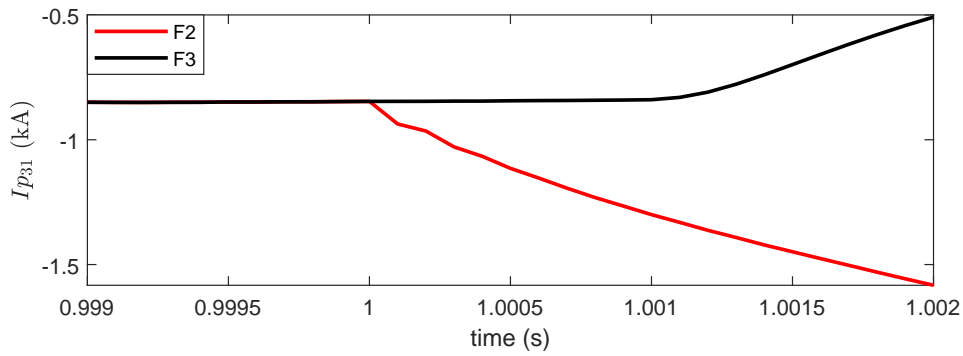


Figure 4.15: I_{p31} during external faults

current-limiting inductor. Moreover, the difference in ROCOC magnitudes can be utilized to distinguish between faults occurring on the protected line and those on adjacent lines or bus faults. Figure 4.16 depicts the resulting $ROCOCP$ observed at R_{31} for the currents depicted in Figure 4.15.

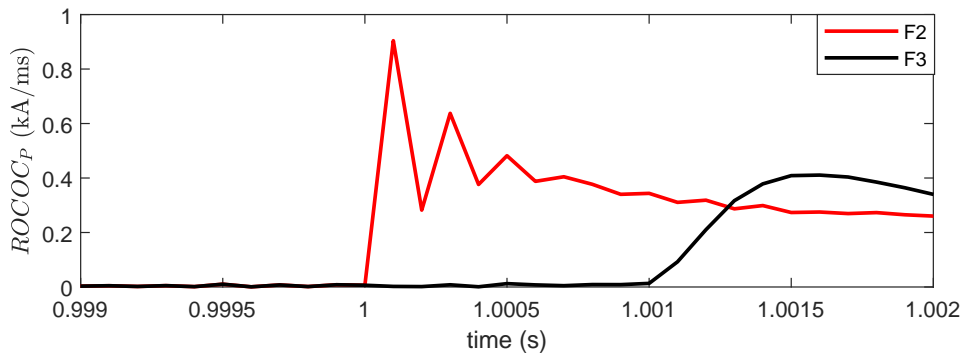


Figure 4.16: $ROCOCP$ during external faults

In summary, the measured $ROCOCP$ and $ROCOCN$ values recorded at R_{31} are compared with their corresponding threshold values, denoted by $ROCOCP_{thresh}$ and $ROCOCN_{thresh}$ respectively. If the recorded $ROCOCP$ or the $ROCOCN$ value cross their respective thresholds, the protection is activated and the faulty branch is isolated. The processes involved in the algorithm have been depicted in Figure 4.17.

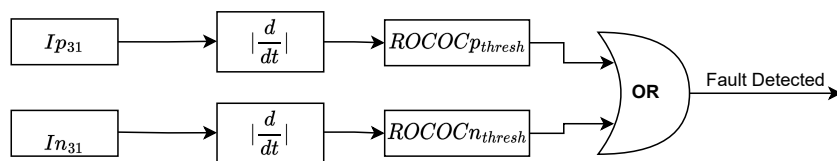


Figure 4.17: ROCOC-based algorithm flowchart

5

Results

5.1. Introduction

This chapter discusses the results of the simulations performed to analyze the performance of the various HVDC protection algorithms. Four different HVDC algorithms' performances have been analyzed in this chapter. The data acquisition and processing for all protection algorithms are performed at the location R_{31} in the test system. The inductance of the terminal inductors at the end of each terminal of the protected line has been set to 40 mH for all simulations. All the faults triggered outside Cable13 are referred to as external faults. A sampling frequency (f_s) of 10kHz has been used for all simulations. All the protection algorithms discussed have been implemented and tested in the PSCAD environment.

In order to test the working of the protection algorithms, a single phase breaker switch was added to each pole of the protected line at R_{13} , as well as R_{31} . When the protection algorithm is activated, a trip signal is sent to the breakers, which then proceed to open and isolate the protected line from the rest of the HVDC network. A breaker status of '0' implies that the breaker is closed, while a breaker status of '1' represents the opening of the breaker. The methodology for analysis follows the same structure for all algorithms. Firstly, the effect of internal faults on the fault determining parameters is investigated, without any protection system in place. The fault-determining parameters for each algorithm are listed as follows:

- Current differential deviation based protection - $\Delta \frac{dI_p}{dt}$, $\Delta \frac{dI_n}{dt}$
- Reactor Voltage-based protection - V_{LT}
- ROCOC based protection - $ROCOCP$, $ROCOCN$
- ROCOV based protection - $ROCOVP$, $ROCOVN$

Figure 5.1 shows the data acquisition points in Cable13. I_{p31} and I_{n31} represent the positive and negative DC line currents at R_{31} . Similarly, I_{p13} and I_{n13} represent the positive and negative DC line currents at R_{13} . V_{p31} and V_{n31} represent the PTG, and NTG voltages measured at R_{31} respectively. V_{LT} represents the voltage across the positive pole terminal inductor at R_{31} .

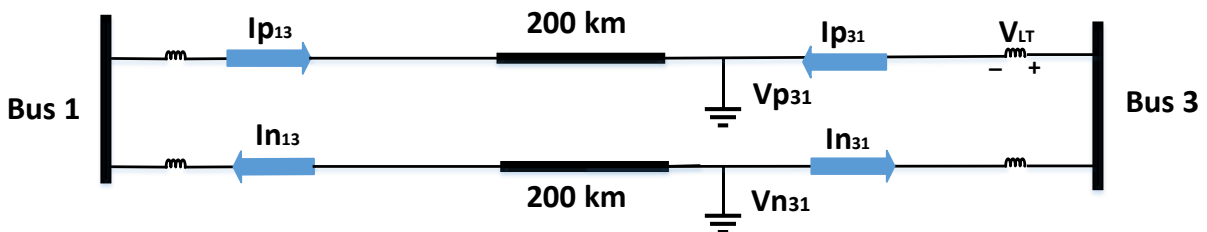


Figure 5.1: Input signals for HVDC protection algorithm

The fault-determining parameters in this thesis have been calculated as follows -

$$\Delta \frac{dI_p}{dt} = \frac{d(I_{p13} + I_{p31})}{dt} \quad (5.1)$$

$$\Delta \frac{dIn}{dt} = \frac{d(In_{13} + In_{31})}{dt} \quad (5.2)$$

$$ROCOV_P = \left| \frac{dV_{p31}}{dt} \right| \quad (5.3)$$

$$ROCOV_N = \left| \frac{dV_{n31}}{dt} \right| \quad (5.4)$$

$$ROCOC_p = \left| \frac{dIp_{31}}{dt} \right| \quad (5.5)$$

$$ROCOC_n = \left| \frac{dIn_{31}}{dt} \right| \quad (5.6)$$

To examine the effect of an internal fault on the fault-determining parameters, a PTG fault, a PTP fault, and an NTG fault, each having a fault distance (x) of 100 km are simulated for each algorithm. x is measured from R_{31} for each simulation. All internal faults have been simulated at $t=1$ s in Cable13, referred to as the protected line. These are represented by f_{13} in Figure 5.2. The performance of the protection algorithm is investigated by analyzing the corresponding breaker status for each fault. For all internal cases, the breaker status is expected to be '1'.

This is followed by a detailed analysis of the protection algorithms under various R_f and x . For the analysis of the effect of R_f , x was set to 100km, and R_f was varied from 0 Ω to 200 Ω . The corresponding value of the fault-determining parameter recorded was noted down along with the time taken for the circuit breaker status to become '1', after the fault inception. This time is referred to as the trip time. Similarly, to analyze the effect of x on each protection algorithm, R_f is fixed at 200 Ω and the x is varied from 10km to 190km. The corresponding fault-determining parameters and the trip times are then recorded.

Furthermore, the effect of external faults on the fault-determining parameters was analyzed. This is followed by an evaluation of the performance of the protection algorithms in the event of external faults, where the breaker status for each external fault case is analyzed. For an ideal protection algorithm, the breaker status should remain '0' for all external fault cases. In this thesis, six different external faults have been simulated to test the selectivity of the protection algorithms. These are labeled as F1,F2,F3,F4,F5 and F6 in Figure 5.2, where

- F1 - PTP fault at cable34
- F2 - AC fault at G1
- F3 - AC fault at G3
- F4 - Remote DC bus fault at Bus4
- F5 - DC Bus fault at Bus1
- F6 - DC Bus fault at Bus3

This is followed by an analysis of the effect of the inductance of the terminal inductors on the protection algorithms. To investigate this effect, a PTG fault having a R_f of 100 Ω and an x of 100km is simulated for five cases for each algorithm. In each case the inductance of the terminal inductors on both ends of the protected line are varied. The analysis is carried out for inductance values of 10 mH, 20 mH, 40 mH, 60 mH, and 80 mH. The noise resilience for each algorithm was then analyzed in MATLAB. Noise with a signal-to-noise ratio (SNR) of 40 dB was added to the input signals for each algorithm. Each algorithm was then realized with the input signals, now containing noise. The methodology implemented for threshold design for the discussed algorithm has been described in this chapter as well. Lastly, the effect of varying the sampling frequency, f_s , on the performance of each protection algorithm is investigated.

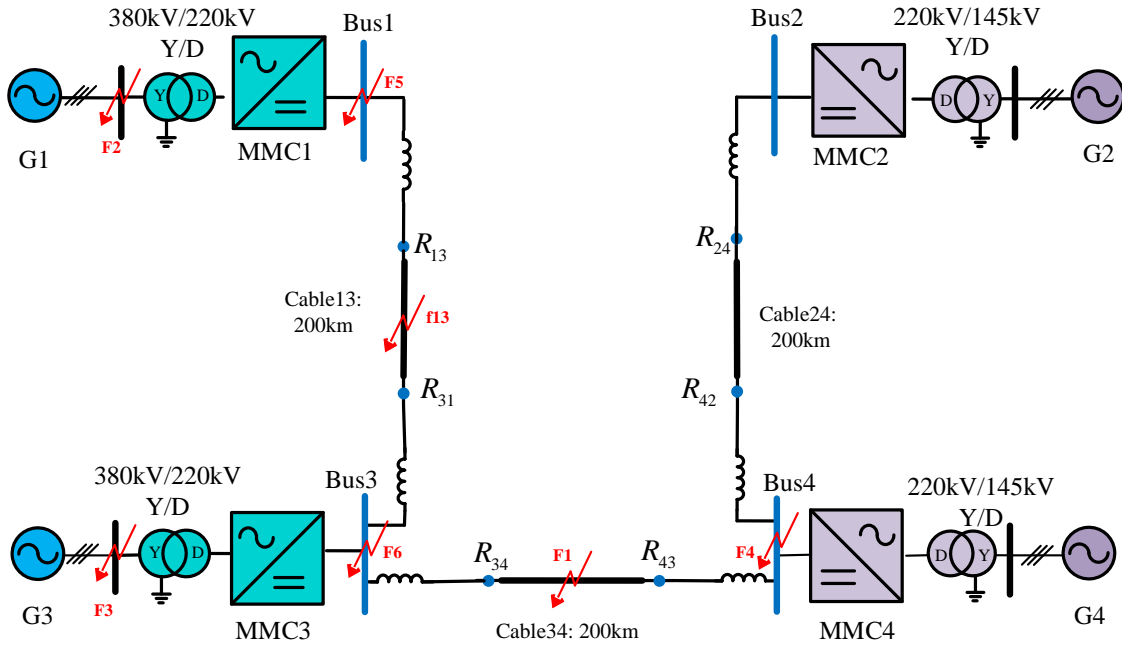


Figure 5.2: Various faults simulated in the HVDC test system

5.2. Current Differential Deviation

5.2.1. Effect of Internal Fault Cases

To examine the effect of internal faults on the current differential deviation, a PTG fault, an NTG fault, and a PTP fault, each having a R_f of $0\ \Omega$ and x of 100 km was simulated. $\Delta \frac{dI_p}{dt}$ and $\Delta \frac{dI_n}{dt}$ recorded for these faults are presented in Figure 5.3 and Figure 5.4 respectively. In both cases, a spike in both $\Delta \frac{dI_p}{dt}$ and $\Delta \frac{dI_n}{dt}$ is observed during an internal fault. From Figure 5.3, it can be seen that the $\Delta \frac{dI_p}{dt}$ is greater than the corresponding $\Delta \frac{dI_n}{dt}$ for a PTG fault. Similarly, in the case of an NTG fault, the $\Delta \frac{dI_n}{dt}$ is found

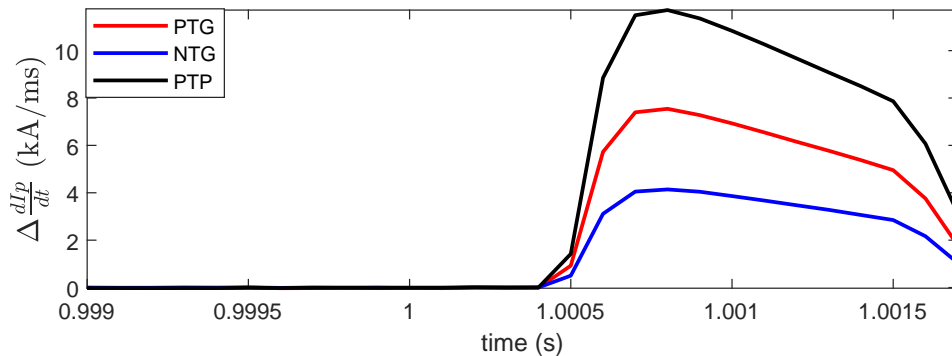


Figure 5.3: $\Delta \frac{dI_p}{dt}$ for internal faults

to be greater than the corresponding $\Delta \frac{dI_p}{dt}$. This can be used to identify the faulty pole in the case of a PTG/NTG fault, providing additional selectivity. The current differential deviation for the PTP fault is found to be greater than that for a PTG and an NTG fault having the same R_f and x . Furthermore, a PTP can be identified if $\Delta \frac{dI_p}{dt}$ and $\Delta \frac{dI_n}{dt}$ are found to be equal. This can be seen in Figure 5.3 and Figure 5.4.

The same internal faults were once again simulated, with the protection algorithm in place. The threshold setting for $\Delta \frac{dI_p}{dt}$ and $\Delta \frac{dI_n}{dt}$ is set as 0.4 kA/ms each. The breaker status for each fault is shown in Figure 5.5. It can be seen that the algorithm successfully triggers the trip signal in the circuit breaker within 0.6 ms of the fault inception time for these internal fault cases.

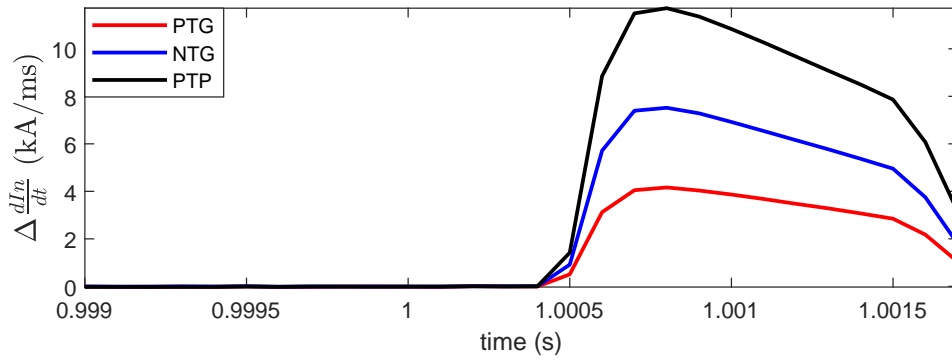


Figure 5.4: $\Delta \frac{dI_n}{dt}$ for internal faults

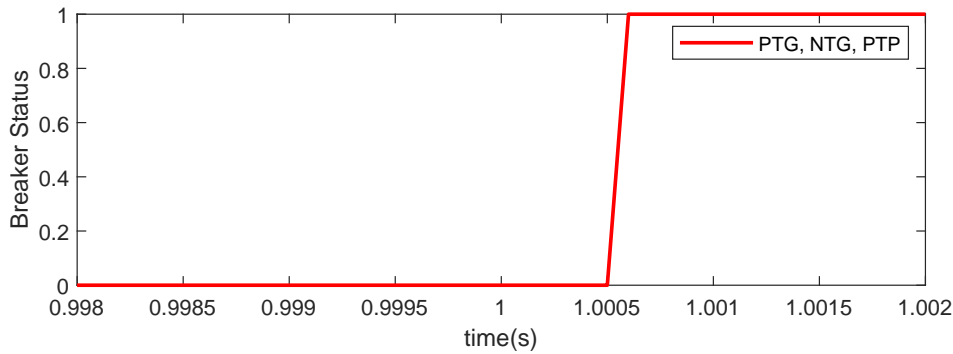


Figure 5.5: Breaker status for internal faults

5.2.2. Effect of Fault Resistance

To test the algorithm's sensitivity to R_f , multiple fault scenarios were simulated with varying R_f . Multiple PTG, NTG, and PTP faults were simulated, with each case having a set R_f . The x was kept constant for each simulation at 100 km. After each simulation, the maximum $\Delta \frac{dI_p}{dt}$, $\Delta \frac{dI_n}{dt}$ was recorded, along with the trip time. Table 5.1 contains the results of the simulations performed. By testing the algorithm's performance under various R_f , the following results were observed. Firstly, when R_f is increased, the current differential deviation observed on both poles decreases. The largest $\Delta \frac{dI_p}{dt}$ for a PTG fault was recorded to be 7.5437 kA/ms, while the largest $\Delta \frac{dI_n}{dt}$ for an NTG fault was found to be 7.5177 kA/ms. Furthermore, the smallest $\Delta \frac{dI_p}{dt}$ for a PTG fault was found to be 0.5821 kA/ms, while the smallest $\Delta \frac{dI_n}{dt}$ for an NTG fault was found to be 0.5720 kA/ms. For PTP faults, the maximum and minimum $\Delta \frac{dI_p}{dt}$ were found to be 11.7111 kA/ms and 1.5763 kA/ms. As the threshold is crossed for $\Delta \frac{dI_p}{dt}$ and $\Delta \frac{dI_n}{dt}$ in all cases, the protection algorithm is successfully activated for all cases. The trip time is found to be increased as R_f is increased for each fault type. The minimum trip time for all fault cases was found to be 0.6 ms while the maximum trip time was found to be 0.7 ms. Thus, the current differential deviation-based algorithm can speedily detect internal faults with R_f up to 200 Ω .

5.2.3. Effect of Fault Distance

To examine the effect of x on the protection algorithm, multiple internal faults were simulated each having a fixed R_f of 200 Ω . The x was then varied from 10 km to 190 km for PTG, NTG, and PTP faults. The results of the simulations have been presented in Table 5.2. The largest $\Delta \frac{dI_p}{dt}$ and $\Delta \frac{dI_n}{dt}$ for all fault cases was recorded for a PTP fault, with an x of 100 km, with a recorded value of 1.5763 kA/ms each. The lowest $\Delta \frac{dI_p}{dt}$ was recorded for a PTG fault with an x of 10 km, at a value of 0.4916 kA/ms. Similarly, it can be seen that the smallest $\Delta \frac{dI_n}{dt}$ was recorded for an NTG fault, with an x of 50 km, at a value of 0.4938 kA/ms. In all cases, $\Delta \frac{dI_p}{dt}$ and $\Delta \frac{dI_n}{dt}$ cross the threshold setting and thus cause the protection algorithm to activate. The longest trip time recorded for PTG and NTG faults is when x is set to 10 km, with a value of 1.2 ms each, while the longest trip time recorded for a PTP fault is when the fault is located at the midpoint of the protected line ($x = 100$ km), with a value of 0.6 ms.

Fault Type	$R_f (\Omega)$	Peak $\Delta \frac{dI_p}{dt}$ (kA/ms)	Peak $\Delta \frac{dI_n}{dt}$ (kA/ms)	Trip Time (ms)
PTG	0	7.5437	4.1638	0.6
	10	4.4428	2.4532	0.6
	50	1.6916	0.9409	0.6
	100	1.0067	0.5347	0.6
	200	0.5821	0.3169	0.7
NTG	0	4.1413	7.5177	0.6
	10	2.4381	4.4257	0.6
	50	0.9353	1.6794	0.6
	100	0.5271	0.9994	0.7
	200	0.3033	0.5720	0.7
PTP	0	11.7111	11.7111	0.6
	10	8.6858	8.6857	0.6
	50	4.2398	4.2398	0.6
	100	2.6005	2.6005	0.6
	200	1.5763	1.5763	0.7

Table 5.1: Effect of fault resistance on Current Differential Deviation-based protection

Thus, the algorithm successfully identifies and is activated for internal faults at all x .

Fault Type	x (km)	Peak $\Delta \frac{dI_p}{dt}$ (kA/ms)	Peak $\Delta \frac{dI_n}{dt}$ (kA/ms)	Trip Time (ms)
PTG	10	0.4916	0.3249	1.2
	50	0.4951	0.3312	0.9
	100	0.5821	0.3169	0.6
	150	0.5640	0.2726	1
	190	0.5796	0.2551	1.1
NTG	10	0.3300	0.4966	1.2
	50	0.3299	0.4938	0.9
	100	0.3033	0.5720	0.7
	150	0.2547	0.5546	0.6
	190	0.2687	0.5998	1.1
PTP	10	1.4895	1.4895	0.2
	50	1.4545	1.4545	0.4
	100	1.5763	1.5763	0.6
	150	1.5075	1.5075	0.4
	190	1.5685	1.5686	0.2

Table 5.2: Effect of fault distance on Current Differential Deviation based protection

5.2.4. Effect of External Fault Cases

Figure 5.6 and figure 5.7 shows the $\Delta \frac{dI_p}{dt}$ and $\Delta \frac{dI_n}{dt}$, observed at R_{31} in the event of external fault cases F1 to F6 without the protection algorithm in place.

The highest recorded $\Delta \frac{dI_p}{dt}$, occurs due to fault case F5, with a value of 0.5242 kA/ms, which is higher than the set threshold of 0.4 kA/ms. The remaining external fault cases generate a lower current differential deviation than the threshold. The results of the simulations performed to analyze the effect of external faults are provided in Table 5.3. Thus, the current differential protection is expected to provide selectivity against faults in neighboring lines and AC faults.

Figure 5.8 shows the breaker status in the event of external faults F1 to F6 after the protection was implemented. Since the threshold value of $\Delta \frac{dI_p}{dt}$ is never crossed for either fault case, the protection remains unactivated. Thus the protection based on current differential deviation provides complete selectivity against all external fault cases.

External fault case	Peak $\Delta \frac{dI_p}{dt}$ (kA/ms)	Peak $\Delta \frac{dI_n}{dt}$ (kA/ms)
F1	-0.0012	-0.0012
F2	0.0185	0.0185
F3	0.0347	0.0347
F4	0.0258	0.0257
F5	0.5242	0.5242
F6	0.3284	0.3284

Table 5.3: Effect of external faults on Current Differential Deviation-based protection

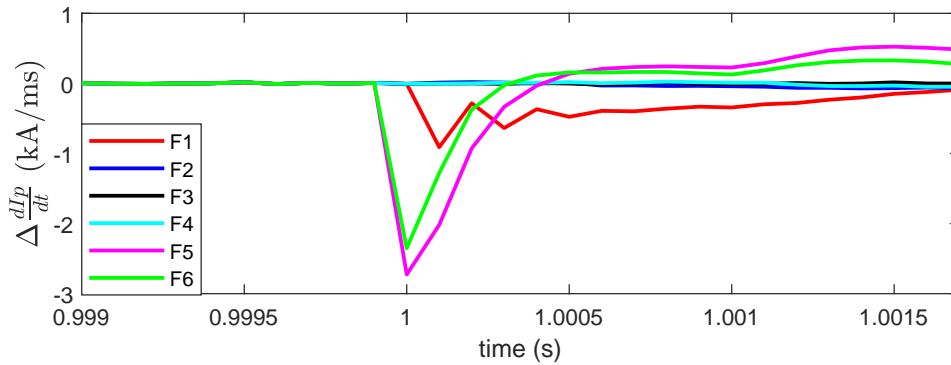


Figure 5.6: $\Delta \frac{dI_p}{dt}$ for external faults

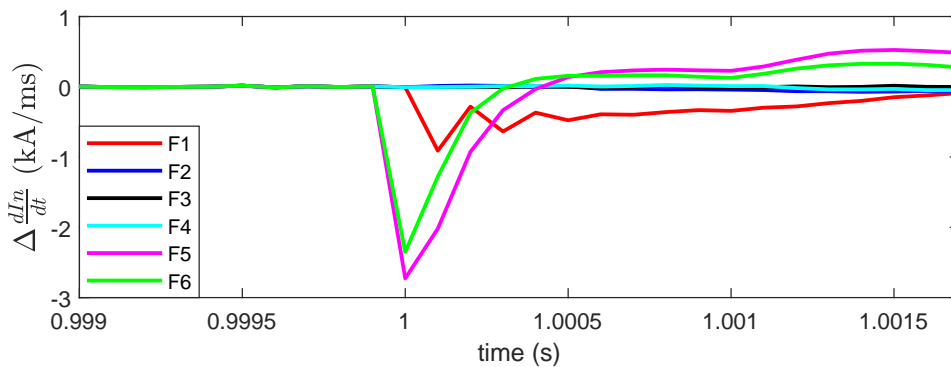


Figure 5.7: $\Delta \frac{dI_n}{dt}$ for external faults

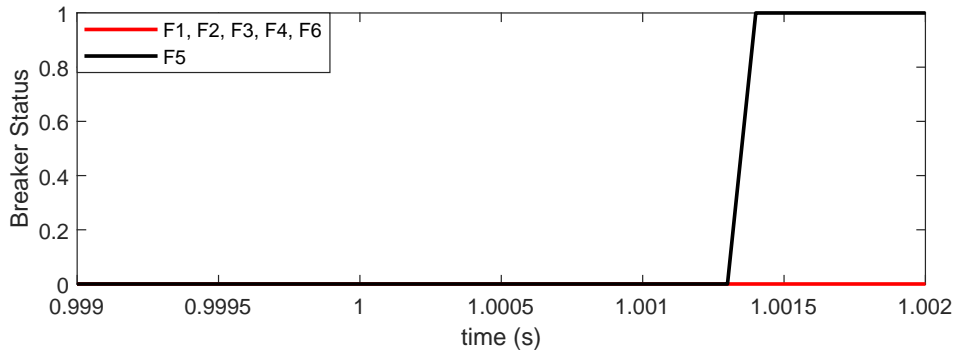


Figure 5.8: Breaker status for external faults

5.2.5. Effect of Terminal Inductor Inductance

To test the effect of varying the terminal inductor's inductance on the protection algorithm, a PTG fault having a fixed R_f of 0Ω and an x of 100 km is simulated for varying inductance levels. The effect of varying the inductance of the terminal inductors on $\Delta \frac{dI_p}{dt}$ is shown in Figure 5.9. The maximum $\Delta \frac{dI_p}{dt}$ recorded decreases as a result of an increase in inductance. Thus, the threshold setting can be lowered when the inductance of the terminal inductors is increased without compromising the security of the HVDC line.

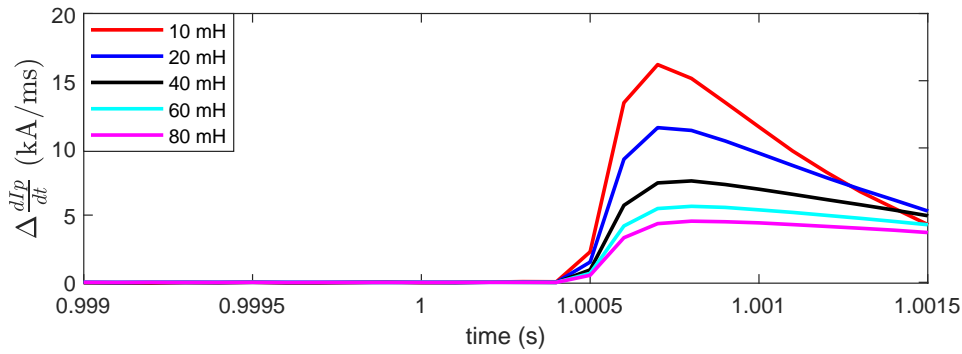


Figure 5.9: $\Delta \frac{dI_p}{dt}$ for a PTG fault with varying terminal inductance

However, due to the small difference for the maximum $\Delta \frac{dI_p}{dt}$ observed for each value of inductance, there is no significant change in trip time observed. As the inductance is increased, $\Delta \frac{dI_p}{dt}$ and $\Delta \frac{dI_n}{dt}$ will take further time to cross the threshold, thus an increase in trip time is expected. Furthermore, a decrease in both the peak $\Delta \frac{dI_p}{dt}$, and $\Delta \frac{dI_n}{dt}$ is observed as the inductance is increased. Table 5.4 shows the results of varying the inductance of the terminal inductors at the ends of the protected line.

Inductance (mH)	Peak $\Delta \frac{dI_p}{dt}$ (kA/ms)	Peak $\Delta \frac{dI_n}{dt}$ (kA/ms)	Trip time (ms)
10	16.1978	11.1380	0.6
20	11.5075	7.1894	0.6
40	7.5437	4.1638	0.6
60	5.6545	2.8649	0.6
80	4.5505	2.1758	0.6

Table 5.4: Effect of inductance on Current Differential Deviation-based protection

5.2.6. Influence Of Noise on Protection Performance

The algorithm's robustness is further tested by introducing white noise in the signal. The input signals for the current differential deviation algorithm are I_{p13} , I_{p31} , I_{n13} and I_{n31} . However, to test the noise resistance of the protection algorithm, a PTG fault is simulated, and only the resulting $\Delta \frac{dI_p}{dt}$ is consid-

ered. $I_{p_{31}}$ and $I_{p_{13}}$ are first measured after triggering a PTG fault ($x = 100 \text{ km}$, $R_f = 100 \Omega$). First, white noise of 40 dB is added to the input signals, as shown in Figure 5.10 and Figure 5.11.

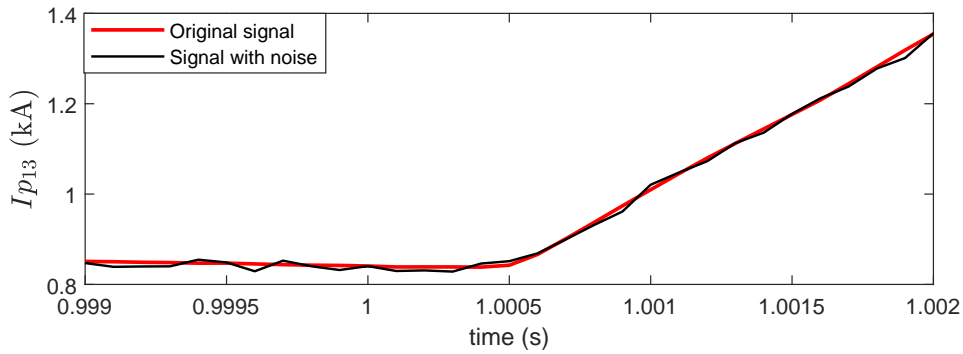


Figure 5.10: $I_{p_{13}}$ with 40dB noise

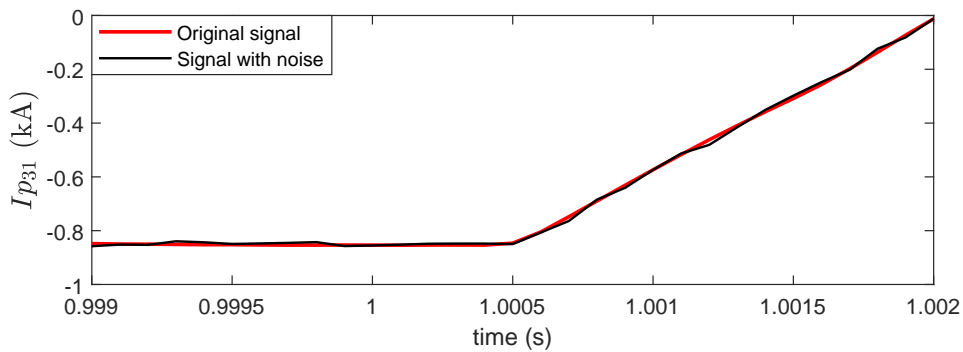


Figure 5.11: $I_{p_{31}}$ with 40dB noise

This is followed by calculating the $\Delta \frac{dI_p}{dt}$ of the current signals after the addition of noise. The result is presented in Figure 5.12. As the maximum $\Delta \frac{dI_p}{dt}$ observed before the fault inception is 0.26 kA/ms, the current differential-based protection can successfully operate under noise having an SNR of 40 or higher.

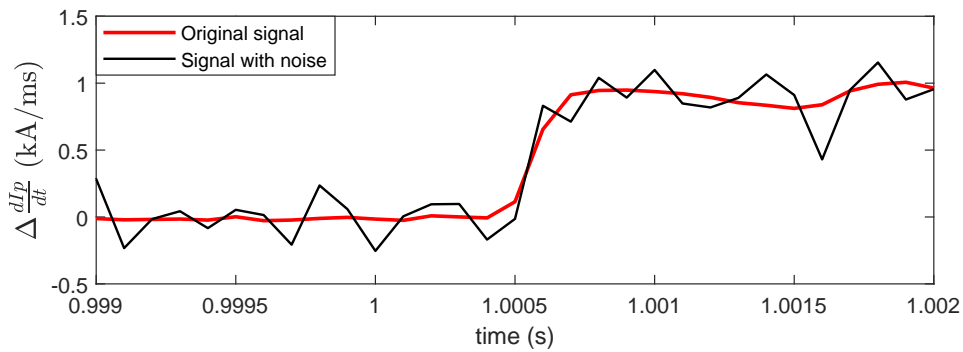


Figure 5.12: $\Delta \frac{dI_p}{dt}$ with 40 dB noise

5.2.7. Threshold Design

The threshold values for the current differential deviation need to be designed in such a way that it is not triggered by the external fault generating the largest current differential deviation, while also successfully activating for the smallest current differential deviation observed during an internal fault. It is evident from the simulation results of the external fault cases, that the resulting current differential deviations observed in the protected line, with the exception of fault case F5, are much lower than the

deviations in internal fault cases. The smallest $\Delta \frac{dI_p}{dt}$ during an internal fault was recorded as 0.4916 kA/ms during a PTG fault with a R_f of 200 Ω and an x of 10 km. The smallest $\Delta \frac{dI_n}{dt}$ observed in the event of an NTG fault ($x = 50$ km, $R_f = 200$ Ω) was 0.4938 kA/ms. These PTG and NTG faults are denoted as F_{PTG} and F_{NTG} respectively in Table 5.5. Thus, the threshold for $\Delta \frac{dI_p}{dt}$ and $\Delta \frac{dI_n}{dt}$ need to be set in such a way that they are less than 0.4916 kA/ms and 0.4938 kA/ms respectively. At the same time, the threshold set should result in idle operation for external faults. As fault case F5 results in a greater $\Delta \frac{dI_p}{dt}$ and $\Delta \frac{dI_n}{dt}$, the external fault with the second highest resulting $\Delta \frac{dI_p}{dt}$ and $\Delta \frac{dI_n}{dt}$ (F6) are considered for threshold setting. The peak $\Delta \frac{dI_p}{dt}$, and $\Delta \frac{dI_n}{dt}$ recorded for this external fault was 0.3284 kA/ms each. In this thesis, a reliability factor of 1.2 is considered for all algorithms [29]. Thus, the threshold for the current differential deviation-based HVDC protection algorithm was set as -

$$\Delta I_{p_{thresh}} = 0.3284 * 1.2 = 0.4 \text{ kA/ms} \quad (5.7)$$

$$\Delta I_{n_{thresh}} = 0.3284 * 1.2 = 0.4 \text{ kA/ms} \quad (5.8)$$

The protection is activated when either $\Delta \frac{dI_p}{dt}$, or $\Delta \frac{dI_n}{dt}$ cross their threshold settings, $\Delta I_{p_{thresh}}$, and $\Delta I_{n_{thresh}}$ respectively.

Fault Type	Peak $\Delta \frac{dI_p}{dt}$ (kA/ms)	Peak $\Delta \frac{dI_n}{dt}$ (kA/ms)
F6	0.3284	0.3284
F_{PTG}	0.4916	0.3249
F_{NTG}	0.3299	0.4938

Table 5.5: Threshold determination of Current Differential Deviation-based protection

5.2.8. Effect of Sampling Frequency

To test the effect of increasing the f_s on the protection algorithm, a PTG fault was triggered ($R_f = 0$ Ω , $x = 100$ km). Table 5.6 presents the results of the investigation. As the f_s is increased, the recorded $\Delta \frac{dI_p}{dt}$ results in a small increase. This is due to the recording of additional data points at the fault instant.

f_s (kHz)	Peak $\Delta \frac{dI_p}{dt}$ (kA/ms)	Peak $\Delta \frac{dI_n}{dt}$ (kA/ms)	Trip time (ms)
10	7.5437	4.1638	0.6
20	7.6027	4.1729	0.6
50	7.6293	4.2011	0.6

Table 5.6: Effect of sampling frequency on Current Differential Deviation-based protection

5.3. ROCOV

5.3.1. Effect of Internal Fault Cases

To examine the effect of internal faults on the ROCOV, three internal faults were triggered, each having a fixed R_f and x of 100 Ω and 100 km respectively. Figure 5.13 shows the effect of these internal faults on the $ROCOV_P$ of the protected line, without the protection algorithm implemented. A large spike in $ROCOV_P$ is observed for the PTG and PTP fault cases at 0.6ms after the fault inception. The maximum $ROCOV_P$ for the PTG fault was found to be 198.776 kV/ms, while the max $ROCOV_P$ for the NTG fault was found to be 18.39 kV/ms. Thus, the ROCOV-based protection algorithm is capable of differentiating the faulty pole from a healthy pole in the event of a single pole-to-ground fault. The max $ROCOV_P$ for the PTP fault was greater than that observed for PTG and NTG faults, with a recorded value of 350.70 kV/ms. Likewise, Figure 5.14 shows the effect of these internal faults on $ROCOV_N$ measured at the protected line, without the protection algorithm implemented. The maximum $ROCOV_N$ for the PTG fault was found to be 18.316 kV/ms, while the max $ROCOV_N$ for the NTG fault was found to be 198.363 kV/ms. The max $ROCOV_N$ for the PTP fault was found to be 350.70 kV/ms. In each fault case, $ROCOV_P$ and $ROCOV_N$ are compared with a threshold of 72 kV/ms. In the event that either $ROCOV_P$ or $ROCOV_N$ crosses the threshold setting, the protection algorithm is activated.

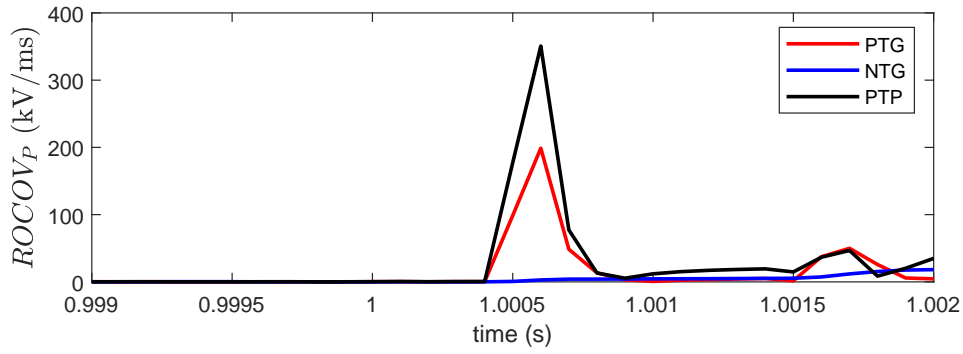


Figure 5.13: $ROCOV_P$ for internal faults

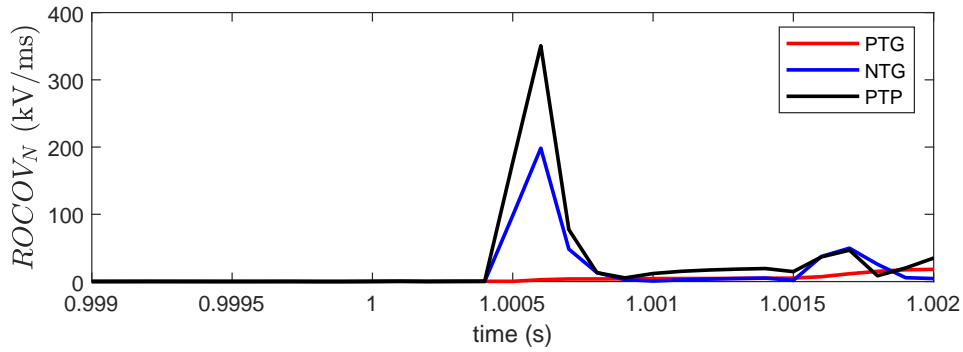


Figure 5.14: $ROCOV_N$ for internal faults

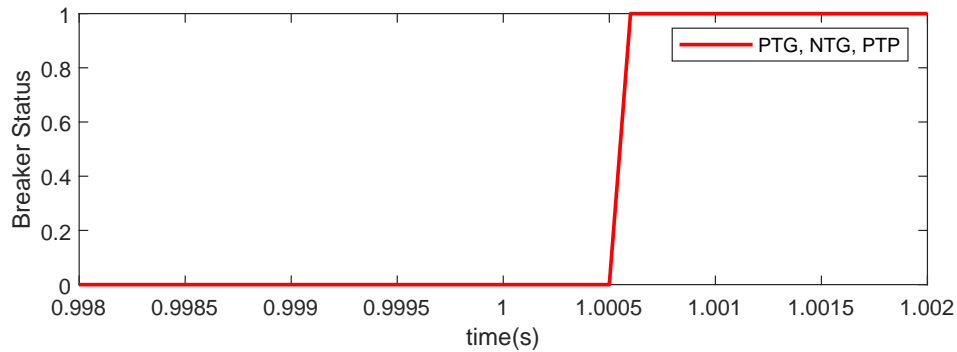


Figure 5.15: Breaker operation for internal faults

In order to test the working of the algorithm, the same internal faults were once again simulated with the algorithm in place. Figure 5.15 shows the breaker status at R_{31} after the protection algorithm was implemented. As expected, the circuit breaker successfully isolated the faulty line when the $ROCOV_P$ and $ROCOV_N$ above the threshold setting was recorded at 0.6 ms for the three internal faults discussed above. Thus, the ROCOV-based algorithm can successfully detect internal faults.

5.3.2. Effect of Fault Resistance

A more detailed analysis of the performance of the algorithm under various internal faults is presented in the following sections. First, the effect of varying R_f on the protection algorithm's performance is investigated. The findings of this investigation are presented in Table 5.7. It can be seen that an increment in R_f results in a drop in $ROCOV_P$ and $ROCOV_N$. The trip time is not affected by R_f values of up to 200 Ω . For all fault cases, the fault detection acts within 0.6 ms. Thus, the ROCOV-based algorithm can accurately and speedily detect internal faults with varying R_f .

Fault Type	$R_f(\Omega)$	Peak $ROCOV_P$ (kV/ms)	Peak $ROCOV_N$ (kV/ms)	Trip Time (ms)
PTG	0	1,659.4	98.87	0.6
	10	957.314	70.46	0.6
	50	355.044	31.039	0.6
	100	198.776	18.39	0.6
	200	105.774	10.069	0.6
NTG	0	99.018	1,657.2	0.6
	10	70.4314	955.9778	0.6
	50	31.00	354.44	0.6
	100	18.316	198.363	0.6
	200	105.4799	10.0189	0.6
PTP	0	1,637.8	1,637.8	0.6
	10	1,198.9	1,198.9	0.6
	50	578.1652	578.1652	0.6
	100	350.70	350.70	0.6
	200	196.403	196.404	0.6

Table 5.7: Effect of fault resistance on ROCOV-based protection

5.3.3. Effect of Fault Distance

In this section, the effect of x , on the performance of the protection algorithm for various internal faults is investigated. The results are presented in Table 5.8. It can be seen that as the x was increased, the resulting peak $ROCOV_P$ and $ROCOV_N$ decreased. However, a more significant effect on the trip time is observed. As the x is increased from 10 km to 190 km, the trip time is increased by 1 ms. Nevertheless, as the longest trip time observed is 1.2 ms, the ROCOV-based protection can be said to effectively detect all internal faults, located anywhere in the line. Other trends observed are the steady decrease in the maximum $ROCOV_P$, and $ROCOV_N$ observed at the faulted pole as the x is increased. Based on the findings from Table 5.7 and 5.8, it is evident that the ROCOV-based protection algorithm can accurately and speedily detect internal faults of any nature.

Fault Type	x (km)	Peak $ROCOV_P$ (kV/ms)	Peak $ROCOV_N$ (kV/ms)	Trip Time (ms)
PTG	10	226.755	4.0850	0.2
	50	180.9122	7.716	0.4
	100	105.7743	10.0698	0.7
	150	79.0338	11.0855	1
	190	100.8311	10.4874	1.2
NTG	10	3.909	227.4059	0.1
	50	7.6962	180.8147	0.3
	100	10.018	105.479	0.6
	150	10.678	78.722	0.8
	190	10.696	100.9282	1
PTP	10	423.6862	423.6863	0.1
	50	337.7780	337.7780	0.3
	100	196.4040	196.4037	0.6
	150	148.3945	148.3949	0.8
	190	182.4259	182.4264	1

Table 5.8: Effect of fault distance on ROCOV-based protection

5.3.4. Effect of External Fault Cases

Figures 5.16 and 5.17 show the effect of external fault cases on the $ROCOV_P$ and $ROCOV_N$, respectively observed on the protected line, without the protection algorithm in place. The $ROCOV_P$ and $ROCOV_N$ observed on the protected line for distant external faults are much lower than that for internal faults. The maximum $ROCOV_P$ and $ROCOV_N$ recorded for these faults is found to be 59.31 kV/ms each for fault case F5. This value is, however, lower than the threshold set for internal fault detection,

thus, the protection algorithm is expected to remain idle for these faults.

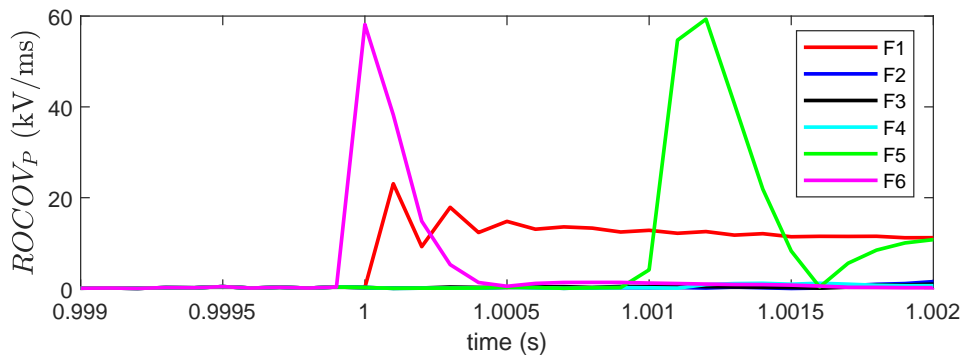


Figure 5.16: $ROCOV_P$ for external faults

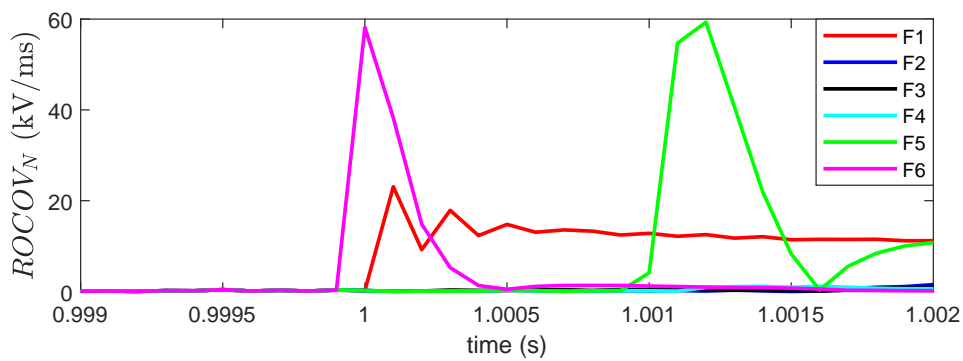


Figure 5.17: $ROCOV_N$ for external faults

External fault case	Peak $ROCOV_P$ (kV/ms)	Peak $ROCOV_N$ (kV/ms)
F1	23.0745	23.0746
F2	1.5135	1.5135
F3	1.1351	1.1344
F4	1.1593	1.1599
F5	59.31	59.3105
F6	58.14	58.14

Table 5.9: Effect of external faults on ROCOV-based protection

Figure 5.18 shows the breaker status of the protected line in the event of external fault cases after the protection algorithm was implemented. As expected based on the analysis above, the protection remains idle for all external fault cases, F1 to F6. This can be seen by the '0' breaker status for these fault cases.

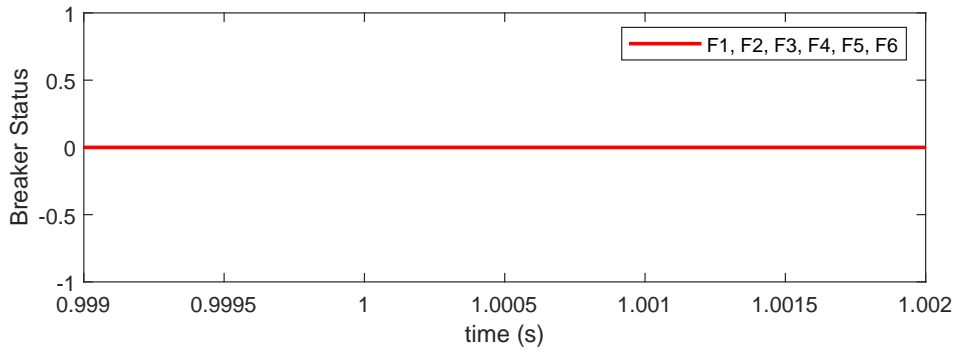


Figure 5.18: Breaker operation for external faults

5.3.5. Effect of Terminal Inductor Inductance

Table 5.10 shows the effect of varying the inductance of the terminal inductors on the $ROCOV_P$ and $ROCOV_N$ in the event of a PTG fault, with x set to 100 km and R_f set to 0Ω . The maximum $ROCOV_P$ was found to be increasing as the inductance of the terminal inductors was increased. The largest $ROCOV_P$ was found to be 1,697.8 kV/ms when the inductance was set as 80 mH, while the smallest $ROCOV_P$ was found to be 1,535.6 kV/ms when the inductance was set as 10 mH. However, as the inductance was increased, a drop in $ROCOV_N$ was observed. The largest peak $ROCOV_N$ recorded was 133.3977 kV/ms, when the inductance was set to 10 mH, while the smallest peak $ROCOV_N$ was found to be 68.02 kV/ms when the inductance was set to 80 mH.

Inductance (mH)	Peak $ROCOV_P$ (kV/ms)	Peak $ROCOV_N$ (kV/ms)	Trip Time (ms)
10	1,535.6	133.3977	0.6
20	1,602.1	119.3365	0.6
40	1,659.4	98.8776	0.6
60	1,683.1	81.1575	0.6
80	1,697.8	68.0243	0.6

Table 5.10: Effect of inductance on ROCOV-based protection

5.3.6. Influence Of Noise on Protection Performance

The robustness of the algorithm is further tested by introducing white noise in the signal. 40 dB noise is first added to the input signal for the algorithm, which is the PTG voltage measured at R_{31} , V_{p31} . Figure 5.19 shows the voltage before and after the noise was added. The voltage signal with the noise added is then used to compute the $ROCOV_P$. The algorithm's performance with white noise having an SNR of 40dB is evaluated. A PTG fault with a R_f of 100Ω at an x of 100km is used to test the noise endurance ability of the algorithm. The results are shown in Figure 5.20.

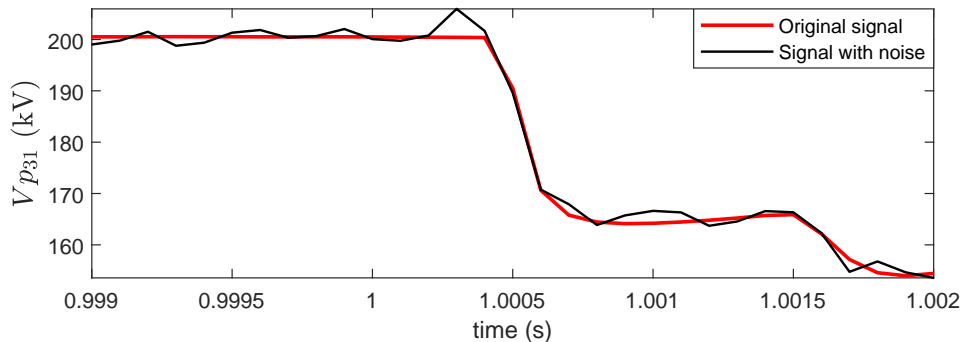


Figure 5.19: V_{p31} with 40 dB noise

While it is evident that the addition of noise to the input signal affects the resultant ROCOV, the

algorithm is still able to accurately detect internal faults, and discriminate them from external faults, as even after the addition of noise in the signal, the threshold of 90 kV/ms is not crossed. While, the ROCOV-based protection can still successfully discriminate internal faults from external faults when noise with an SNR of 40 dB is added, as the SNR of the noise added is decreased, the protection algorithm will fail to distinguish internal faults from normal operating conditions, and thus the performance of the algorithm will be compromised.

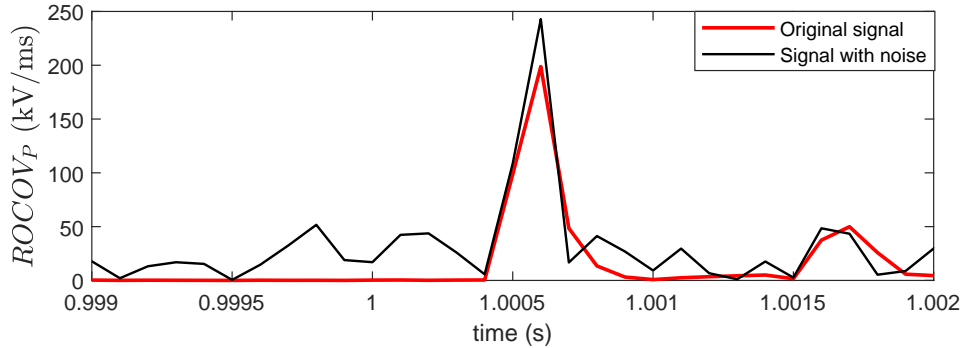


Figure 5.20: $ROCOV_P$ with 40 dB noise

5.3.7. Threshold Design

To set the threshold for accurate fault detection, the largest peak $ROCOV_P$, and $ROCOV_N$ for an external fault, and the smallest peak $ROCOV_P$, and $ROCOV_N$ for an internal fault are noted. For PTG faults, the smallest $ROCOV_P$ is considered while for NTG faults, the smallest $ROCOV_N$ is considered. The largest $ROCOV_P$ and $ROCOV_N$ for an external fault was obtained from the external fault case F5, a DC bus fault at Bus 1. The maximum $ROCOV_P$ and $ROCOV_N$ observed for this fault is 59.31 kV/ms each. The smallest peak $ROCOV_P$ for a PTG fault was found to be 79.0338 kV/ms, while the smallest peak $ROCOV_N$ for an NTG fault was found to be 78.722 kV/ms. In both cases, x was set to 150 km and R_f was set to 200 Ω . These PTG and NTG faults have been labeled as F_{PTG} , and F_{NTG} respectively in Table 5.11. Thus, the threshold setting for $ROCOV_P$ ($ROCOV_{pthresh}$) needs to be set such that it is greater than 59.31 kV/ms, and less than 79.0338 kV/ms. Similarly, the threshold for $ROCOV_N$ ($ROCOV_{nthresh}$) should be set such that it is greater than 59.31 kV/ms and less than 78.72 kV/ms. Considering a reliability factor of 1.2, $ROCOV_{pthresh}$ and $ROCOV_{nthresh}$, are calculated as follows.

$$ROCOV_{pthresh} = 1.2 * 59.31 = 71.18 \text{ kV/ms} \quad (5.9)$$

$$ROCOV_{nthresh} = 1.2 * 59.31 = 71.18 \text{ kV/ms} \quad (5.10)$$

Thus a threshold of 72 kV/ms is selected for $ROCOV_P$, as well as $ROCOV_N$. The protection is activated if either $ROCOV_P$ or $ROCOV_N$ crosses this threshold.

Fault type	Peak $ROCOV_P$ (kV/ms)	Peak $ROCOV_N$ (kV/ms)
F5	59.31	59.31
F_{PTG}	79.0338	11.0855
F_{NTG}	10.678	78.722

Table 5.11: Threshold determination of ROCOV-based protection

5.3.8. Effect of Sampling Frequency

To analyze the effect of the f_s on the ROCOV-based protection, a PTG fault ($x = 100$ km, $R_f = 100 \Omega$) was simulated with varying sampling frequencies. Table 5.12 shows the results of the investigation. It can be seen that as the f_s is increased, the first data point crossing the threshold is detected earlier, thus a reduction in trip time is observed.

f_s (kHz)	Peak $ROCOV_P$	Peak $ROCOV_N$	Trip Time (ms)
10	1,659.4	98.8776	0.6
20	3,108.3	99.7148	0.55
50	5,141.4	100.3743	0.54

Table 5.12: Effect of sampling frequency on ROCOV-based protection

5.4. ROCOC

5.4.1. Effect of Internal Fault Cases

To examine the effect of internal faults on the ROCOC of the line, a PTP, PTG, and an NTG fault were triggered, without the protection algorithm in place. R_f and x for each fault were set to 0Ω and 100 km respectively. The corresponding $ROCO_C_P$, and $ROCO_C_N$ measured at R_{31} was recorded. Figure 5.21 shows the observed $ROCO_C_P$ in the event of various internal faults, while Figure 5.22 shows the observed $ROCO_C_N$ in the event of internal faults. A sharp rise in the $ROCO_C_P$ and $ROCO_C_N$ is observed for all three internal fault cases within 0.6ms of fault inception. The maximum $ROCO_C_P$ and $ROCO_C_N$ recorded for the PTP fault was found to be 6.0615 kA/ms each. The maximum $ROCO_C_P$ recorded for the PTG and NTG faults were found to be 4.7189 kA/ms and 1.331 kA/ms respectively. Furthermore, the maximum $ROCO_C_N$ recorded for the PTG and NTG faults were 1.1392 kA/ms and 4.7074 kA/ms respectively. The threshold for $ROCO_C_P$, and $ROCO_C_N$ is set at 0.05 kA/ms each. If $ROCO_C_P$ or $ROCO_C_N$ of above 0.5 kA/ms is recorded at R_{31} , the protection algorithm is triggered, sending a trip signal to the breaker.

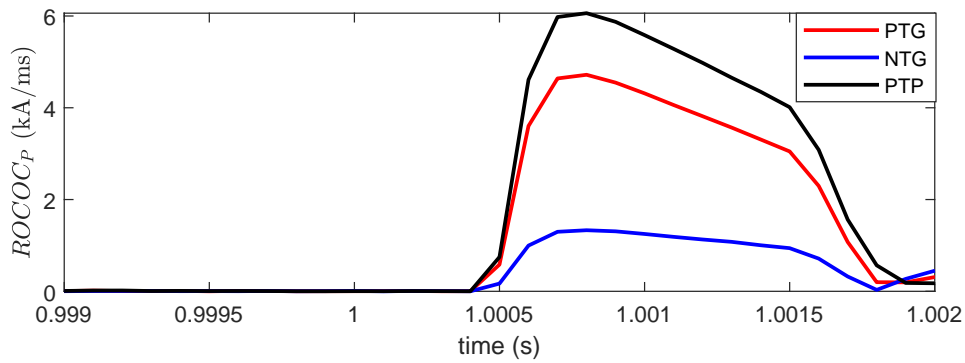


Figure 5.21: $ROCO_C_P$ for internal faults

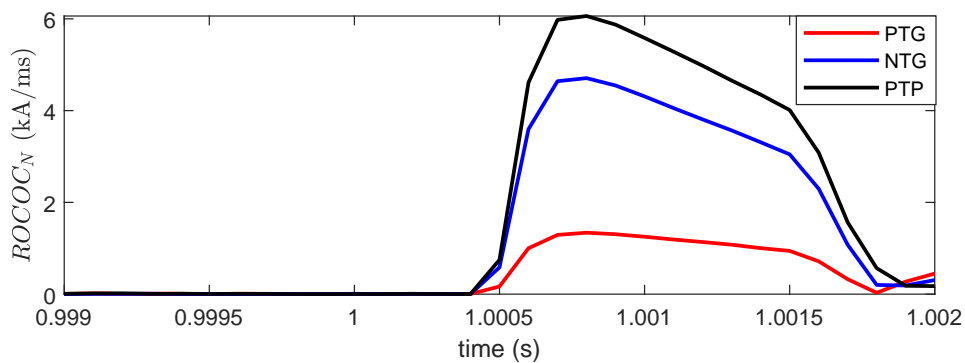


Figure 5.22: $ROCO_C_N$ for internal faults

Once, the protection algorithm was in place, the same three internal faults were once again simulated while the breaker status was monitored. Figure 5.23 shows the breaker status for all three faults. The trip time recorded for each fault case was 0.6 ms. It can be seen that for all fault cases, the protection is successfully activated within 1 ms of fault inception.

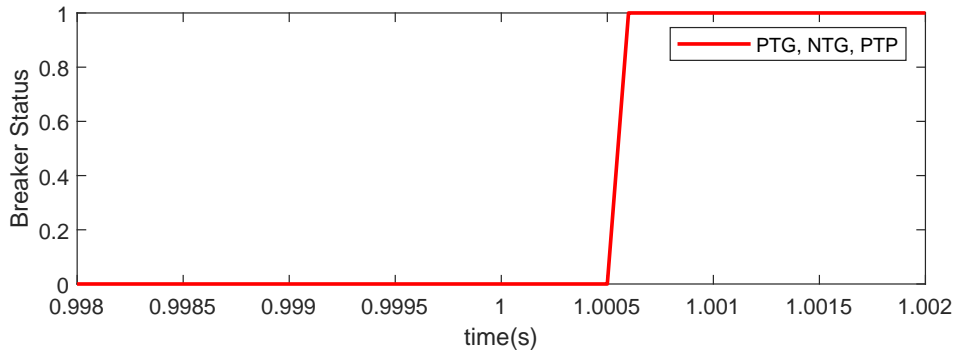


Figure 5.23: Breaker operation for internal faults

5.4.2. Effect of Fault Resistance

Table 5.13 shows the simulation results of the response of the algorithm under various R_f for PTG, NTG, and PTP faults. The x is fixed at 100km. The maximum $ROCOCP$, and $ROCOCN$ observed showed a decline for all fault types as R_f was increased. For PTG and NTG faults, an increase in the tripping time was observed. The longest trip time recorded was 0.8 ms while the smallest peak $ROCOCP$ and $ROCOCN$ were recorded as 0.1018 kA/ms and 0.1014 kA/ms respectively. As these are greater than the threshold set, the ROCOC-based method successfully detects internal faults speedily with a R_f of up to 200 Ω .

Fault Type	$R_f(\Omega)$	Peak $ROCOCP$ (kA/ms)	Peak $ROCOCN$ (kA/ms)	Trip Time (ms)
PTG	0	4.7189	1.3392	0.6
	10	2.7782	0.7886	0.6
	50	1.0544	0.3038	0.6
	100	0.6350	0.1691	0.7
	200	0.3572	0.1014	0.8
NTG	0	1.331	4.7074	0.6
	10	0.7783	2.7658	0.6
	50	0.3038	1.0536	0.6
	100	0.1651	0.6311	0.7
	200	0.1018	0.3533	0.8
PTP	0	6.0615	6.0615	0.6
	10	4.4997	4.4997	0.6
	50	2.1961	2.1961	0.6
	100	1.3449	1.3449	0.6
	200	0.8007	0.8007	0.6

Table 5.13: Effect of fault resistance on ROCOC-based protection

5.4.3. Effect of Fault Distance

As the x was increased, the time taken for the protection algorithm to activate increased significantly. The protection acts speedily for faults close to the relay, with a resultant trip time of 0.2 ms for PTG/NTG faults having an x of 10 km. For PTG/NTG faults at the end of the line, the tripping signal was received 1.2ms after fault inception. PTP faults are detected faster than the PTG/NTG faults having the same x and R_f . For PTP faults having an x of 10 km, the trip time recorded was 0.1 ms, while the longest trip time was recorded at 1.1 ms, for a fault with an x of 190 km.

Fault Type	x (km)	Peak $ROCOCP$ (kA/ms)	Peak $ROCOCN$ (kA/ms)	Trip Time (ms)
PTG	10	0.3867	0.1196	0.2
	50	0.3653	0.1114	0.4
	100	0.3572	0.1014	0.7
	150	0.4254	0.1029	1
	190	0.4312	0.1036	1.2
NTG	10	0.1025	0.3741	0.2
	50	0.1058	0.3598	0.4
	100	0.1018	0.3533	0.7
	150	0.1035	0.4220	0.9
	190	0.1118	0.4367	1.2
PTP	10	0.8778	0.8778	0.1
	50	0.8496	0.8496	0.3
	100	0.8007	0.8007	0.6
	150	0.9779	0.9779	0.9
	190	0.9891	0.9891	1.1

Table 5.14: Effect of fault distance on ROCOC-based protection

5.4.4. Effect of External Fault Cases

To analyze the effect of external faults on the $ROCOCP$, and $ROCOCN$, six external fault cases were simulated while the maximum $ROCOCP$, and $ROCOCN$ observed at R_{31} were monitored. The protection algorithm had not been implemented during the simulation of these faults. Figure 5.24, Figure 5.25, and Table 5.15 show the results of the simulations. The largest peak $ROCOCP$ and $ROCOCN$ are recorded in the event of F6, at 1.273 kA/ms each. Additionally, fault cases F5 and F1 result in an $ROCOCP$, and $ROCOCN$ greater than the threshold. Thus, the ROCOC-based algorithm is expected to not be triggered for fault cases F2, F3, and F4 while it is expected to give be falsely triggered for fault cases F1, F5, and F6.

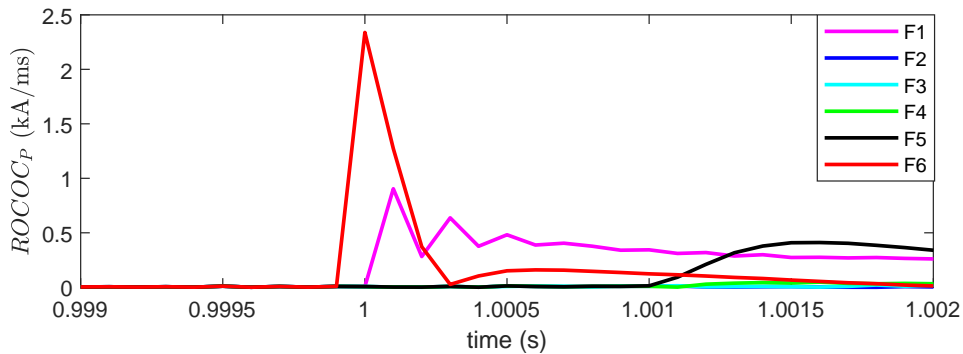


Figure 5.24: $ROCOCP$ for external faults

External fault case	Peak $ROCOCP$ (kA/ms)	Peak $ROCOCN$ (kA/ms)
F1	0.981	0.981
F2	0.0123	0.0123
F3	0.0272	0.0272
F4	0.0472	0.0472
F5	0.4107	0.4107
F6	2.3384	2.3384

Table 5.15: Effect of external faults on ROCOC-based protection

The same six external faults were once again simulated with the protection algorithm in place. The breaker status was monitored for each case. Figure 5.26 shows the breaker status for each external fault case. As the threshold setting is only crossed for fault case F5, the protection is only triggered

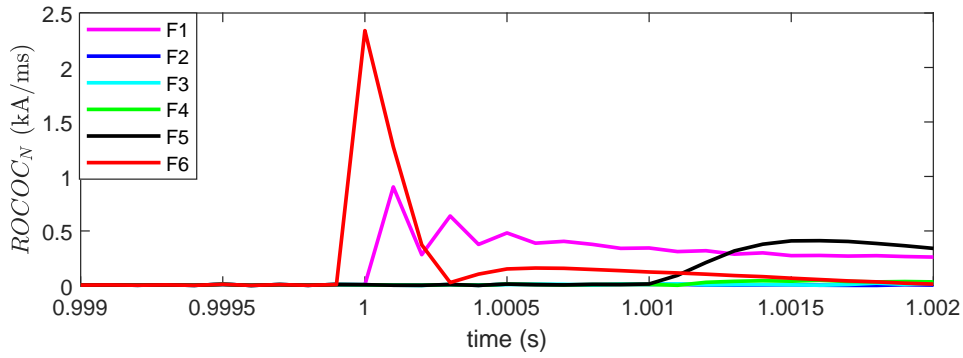


Figure 5.25: $ROCOC_N$ for external faults

for that fault. Thus, the ROCOC-based protection offers selectivity against AC faults, remote DC bus faults, and faults in neighboring lines.

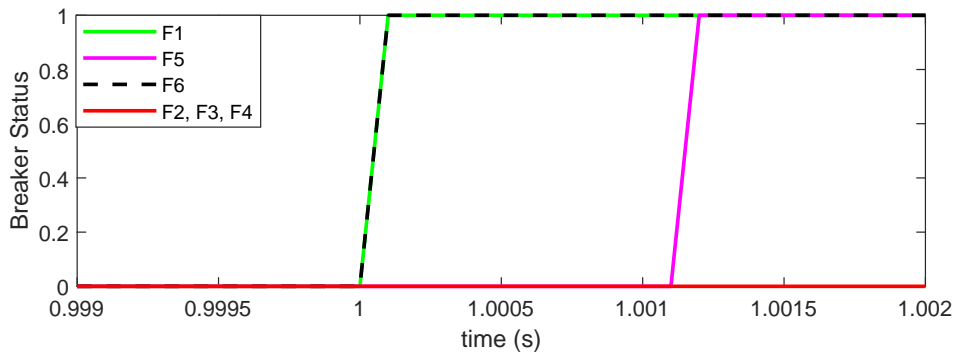


Figure 5.26: Breaker operation for external faults

5.4.5. Effect of Terminal Inductor Inductance

To analyze the effect of the inductance of the terminal inductors on $ROCOCP$, and $ROCOCN$ as well as the performance of the algorithm, a PTG fault having a fixed R_f of 0Ω , and an x of 100km was simulated. The inductance of the terminal inductors was varied for each simulation. Table 5.16 show the results for each simulation. Figure 5.27 shows the effect of varying inductances on the $ROCOCP$, and $ROCOCN$ during a PTG fault. The maximum recorded $ROCOCP$, and $ROCOCN$ decreases as the inductance is increased.

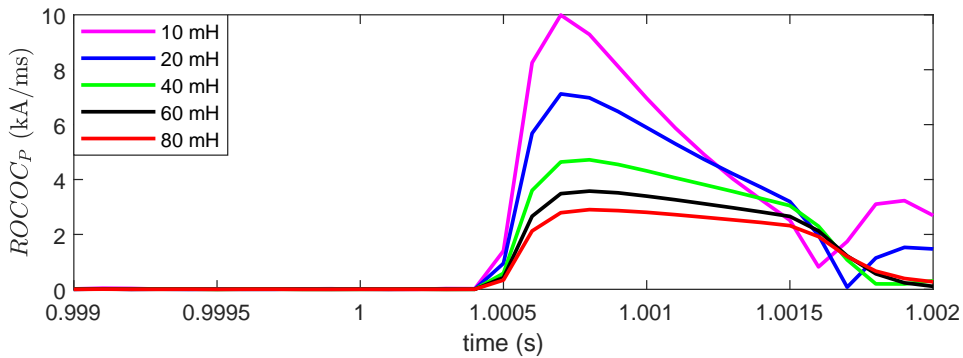


Figure 5.27: $ROCOCP$ during internal faults with varied terminal inductance

Inductance (mH)	Peak $ROCOC_P$ (kA/ms)	Peak $ROCOC_N$ (kA/ms)	Trip Time (ms)
10	9.9923	4.9328	0.6
20	7.1186	2.8007	0.6
40	4.7189	1.3392	0.6
60	3.5780	0.8024	0.6
80	2.9033	0.5510	0.6

Table 5.16: Effect of inductance on ROCOC-based protection

5.4.6. Influence Of Noise on Protection Performance

To analyze the robustness of the algorithm against noise, white noise having an SNR of 40 dB was injected into the input signal of the algorithm, which is the DC line current measured at R_{31} . Figure 5.28 shows the original current signal measured at the positive pole at R_{31} , I_{p31} along with the noisy signal. For this analysis, a PTG fault having a R_f of 100 Ω and an x of 100 km was simulated. The effect of noise on the $ROCOC_P$ is shown in Figure 5.29.

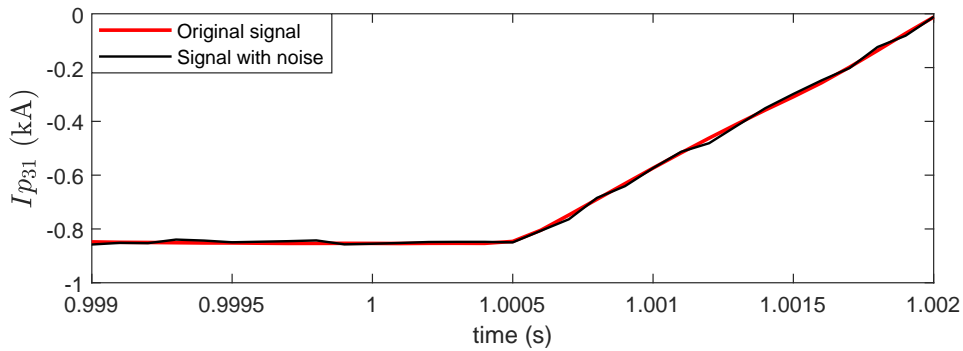


Figure 5.28: I_{p31} with 40 dB noise

Due to the $ROCOC_P$ crossing the threshold under normal operating conditions, as shown in Figure 5.29, the algorithm will be falsely activated. Thus, it is evident that the ROCOC-based method is vulnerable to noise and cannot operate accurately in the presence of noise having an SNR of 40 dB or lower.

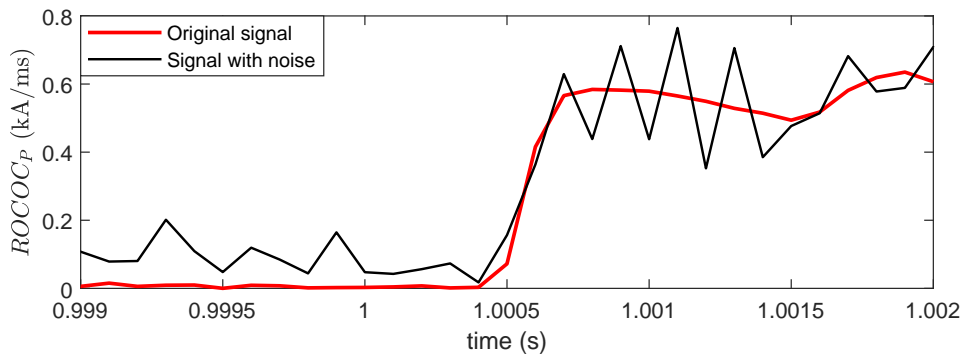


Figure 5.29: $ROCOC_P$ with 40 dB noise

5.4.7. Threshold Design

The protection algorithm should be triggered for the smallest $ROCOC_P$ and $ROCOC_N$ observed for an internal fault while ignoring external faults resulting in the largest $ROCOC_P$ and $ROCOC_N$ on the protected line. The smallest $ROCOC_P$ recorded for a PTG fault was 0.3572 kA/ms, while the smallest $ROCOC_N$ for an NTG fault was 0.3533 kA/ms. These PTG and NTG faults have been labeled as F_{PTG} and F_{NTG} in table 5.17. Among the six external fault cases, F6 resulted in the largest $ROCOC_P$ and $ROCOC_N$ recorded on the protected line, with a value of 1.273 kA/ms each. Furthermore, fault cases

F1 and F5 resulted in $ROCOCP$, and $ROCOCN$ greater than the smallest $ROCOCP$, and $ROCOCN$ observed during an internal fault. Thus the algorithm will generate a false trip signal for fault cases F1, F5, and F6. Thus, the algorithm can discriminate internal faults from fault cases F2, F3, and F4. Among these fault cases, F4 results in the largest $ROCOCP$ and $ROCOCN$ (0.0472 kA/ms). The threshold value for the $ROCOCP$ and $ROCOCN$ needs to be set in such a way that it is larger than 0.0472 kA/ms. A reliability factor of 1.2 is chosen. Thus the thresholds for the ROCOC-based algorithm, $ROCOCP_{thresh}$, and $ROCOCN_{thresh}$ are set as follows -

$$ROCOCP_{thresh} = 1.2 * 0.0472 = 0.05 \text{ kA/ms} \quad (5.11)$$

$$ROCOCN_{thresh} = 1.2 * 0.0472 = 0.05 \text{ kA/ms} \quad (5.12)$$

The threshold in this thesis was thus chosen to be 0.05 kA/ms. The protection is activated when either $ROCOCP$ or $ROCOCN$ crosses this threshold. Table 5.17 shows the simulation results for threshold determination.

Fault Type	Peak $ROCOCP$ (kA/ms)	Peak $ROCOCN$ (kA/ms)
F4	0.0472	0.0472
F_{PTG}	0.3572	0.1014
F_{NTG}	0.1018	0.3533

Table 5.17: Threshold determination of ROCOC-based protection

5.4.8. Effect of Sampling Frequency

Table 5.18 shows the resulting $ROCOCP$, $ROCOCN$ and the trip time observed for a PTG fault ($R_f = 0 \Omega$, $x = 100$ km) with varying f_s . As the f_s was increased, the first data point crossing the threshold was encountered earlier by the algorithm, this can be seen in the decreasing trip time as the f_s was increased.

f_s (kHz)	Peak $ROCOCP$ (kA/ms)	Peak $ROCOCN$ (kA/ms)	Trip Time (ms)
10	4.7189	1.3392	0.6
20	4.7626	1.3406	0.55
50	4.7785	1.3505	0.54

Table 5.18: Effect of sampling frequency on ROCOC-based protection

5.5. DC Reactor Voltage Change Rate

5.5.1. Effect of Internal Fault Cases

The main fault detection condition in this algorithm is the time taken for the terminal reactor voltage to reach voltage threshold V_{LT2} from V_{LT1} . V_{LT1} and V_{LT2} have been set as 5 kV and 8 kV respectively in this thesis. The time taken for the reactor voltage to cross V_{LT1} is represented as $t1$ while the time taken for the reactor voltage to cross V_{LT2} is represented as $t2$. The time difference between $t2$ and $t1$ is represented as Δt . The main working principle of the algorithm is that for relevant fault cases, the observed Δt is lower than the threshold value set for Δt . The threshold for Δt is set as 0.25 ms for all simulations. To investigate the effect of internal faults on the reactor voltage, three internal faults were simulated. Each fault had a R_f of 0 Ω and an x of 100 km. Figure 5.30 shows the reactor voltage recorded for these internal faults.

In all three cases, the reactor voltage crosses 8 kV, thus the thresholds V_{LT1} and V_{LT2} are satisfied. The Δt values recorded for the PTG, NTG, and PTP faults are 0.1ms, 0.1ms, and 0ms respectively. As the Δt values are less than the threshold, the algorithm is expected to be triggered for these internal fault cases. The same three internal faults were once again triggered with the reactor voltage-based protection algorithm in place. Figure 5.31 shows the breaker status in the event of internal faults. The trip time recorded for the PTP fault, NTG fault, and PTG fault was found to be 0.6 ms. Thus, the reactor voltage-based algorithm is successfully able to identify internal faults.

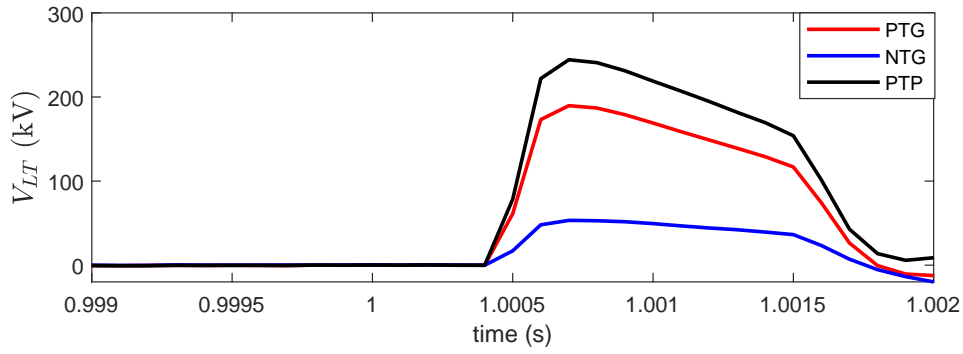


Figure 5.30: V_{LT} for internal faults

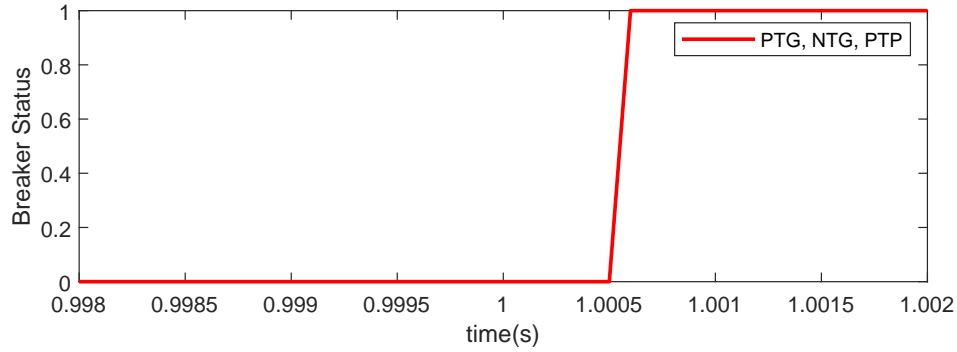


Figure 5.31: Breaker operation for internal faults

5.5.2. Effect of Fault Resistance

To investigate the effect of R_f on the reactor voltage-based protection algorithm, multiple internal faults having a fixed x of 100km were simulated with varying R_f . The results have been presented in Table 5.19. For PTG and NTG faults, it can be seen that as R_f is increased, an increase in t_1 as well as t_2 is observed. For PTG faults, the smallest t_1 recorded was 0.5 ms, when R_f was set as 0 Ω . The longest t_1 recorded for a PTG fault was 0.6 ms when R_f was set to 200 Ω . Similar results are observed for t_2 . For PTG faults, the smallest t_2 recorded was 0.5 ms, when R_f was set to 0 Ω , while the largest t_2 recorded was 0.8 ms when R_f was set to 200 Ω . Likewise, for the NTG faults, the smallest and largest t_1 recorded were 0.5 ms and 0.6 ms respectively. The smallest and largest t_2 recorded for an NTG fault was 0.5 ms and 0.8 ms respectively. The algorithm however, observes no such delays for PTP faults having R_f up to 100 Ω , as all the PTP faults simulated result in a recorded Δt of 0 ms, with t_1 and t_2 being 0.5 ms. However, when the R_f is set to 200 Ω , t_1 and t_2 are recorded as 0.5 and 0.6 ms, respectively. Thus, Δt is found to be 0.1 ms for this case.

5.5.3. Effect of Fault Distance

The effect of x on this protection algorithm is similar to that of R_f . As the x is increased, the time taken for the reactor voltage to cross the V_{LT1} and V_{LT2} increases for all fault types. The same is true for Δt as well, for all fault cases. The smallest value of t_1 and t_2 were recorded at 0.1 ms each, with an x of 10 km for all fault types, while the largest value of t_1 and t_2 was recorded as 1.1 ms and 1.2 ms respectively, with the x set at 190 km. As a result of the delay in the crossing of the voltage thresholds, the trip time increases as the x is increased. The longest trip time recorded was 1.2 ms for PTG and NTG faults, while the longest trip time observed for a PTP fault was found to be 1.1 ms. Thus, the reactor voltage-based protection algorithm successfully detects internal faults at all x .

Fault Type	$R_f(\Omega)$	Peak $V_{LT}(kV)$	t1 (ms)	t2 (ms)	Δt (ms)	Trip Time (ms)
PTG	0	189.6873	0.5	0.5	0	0.6
	10	110.9378	0.5	0.5	0	0.6
	50	42.1879	0.5	0.5	0	0.6
	100	25.1067	0.5	0.5	0	0.6
	200	14.1797	0.5	0.5	0	0.6
NTG	0	53.2525	0.5	0.5	0	0.6
	10	31.1647	0.5	0.5	0	0.6
	50	12.1281	0.5	0.5	0	0.6
	100	6.7844	0.5	0.5	0	0.6
	200	4.1747	0.5	0.5	0	0.6
PTP	0	244.3141	0.5	0.5	0	0.6
	10	179.5600	0.5	0.5	0	0.6
	50	88.2292	0.5	0.5	0	0.6
	100	53.8879	0.5	0.5	0	0.6
	200	32.2184	0.5	0.5	0	0.6

Table 5.19: Effect of fault resistance on DC Reactor Voltage Change Rate-based protection

Fault Type	x (km)	Peak V_{LT} (kV)	t1(ms)	t2(ms)	Δt	Trip Time (ms)
PTG	10	17.3224	0.1	0.1	0	0.2
	50	16.9520	0.3	0.3	0	0.5
	100	14.1797	0.5	0.5	0	0.8
	150	14.6770	0.8	0.8	0	1.1
	190	15.6767	1	1	0	1.2
NTG	10	4.1153	0.1	0.1	0	0.2
	50	4.2536	0.3	0.3	0	0.4
	100	4.1747	0.5	0.5	0	0.7
	150	3.9119	0.8	0.8	0	1.1
	190	4.5082	1	1	0	1.2
PTP	10	37.6463	0.1	0.1	0	0.1
	50	33.9891	0.3	0.3	0	0.3
	100	32.2184	0.5	0.5	0	0.5
	150	39.0498	0.8	0.8	0	0.8
	190	39.3628	1.0	1	0	1.1

Table 5.20: Effect of fault distance on DC Reactor Voltage Change Rate-based protection

5.5.4. Effect of External Fault Cases

Figure 5.32 shows the effect of external fault cases F1 to F6 on the reactor voltage. The protection algorithm has not been implemented for the simulation of these faults. The peak reactor voltage is found to be 8.23 kV/ms for fault case 'F6'. As none of the fault cases result in the crossing of V_{LT2} , the protection algorithm is expected to remain idle for fault cases F1 to F6.

The six external fault cases were once again simulated with the reactor voltage-based protection algorithm implemented. As expected, due to the voltage thresholds not being crossed in fault cases F1 to F4, the protection algorithm is not activated. In fault case F5, the resulting Δt was found to be 0.1 ms. As this is greater than the Δt threshold of 0.0833 ms, the protection is expected to remain idle. However, for fault case F6, Δt was found to be 0 ms. Thus the breaker status is observed to be '0' for all external fault cases, except F6.

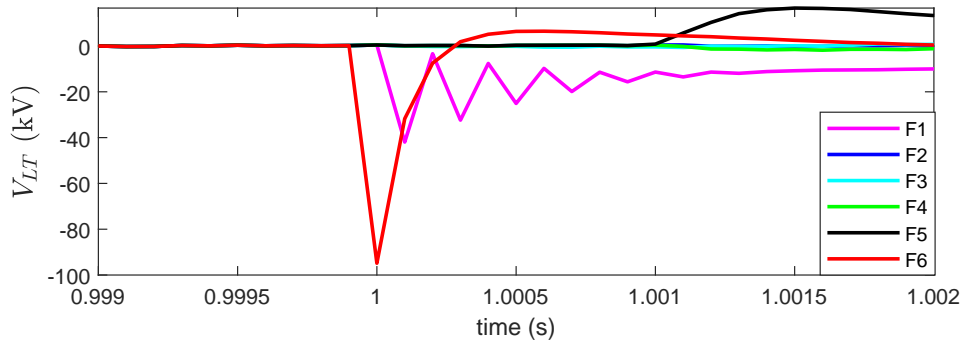


Figure 5.32: V_{LT} for external faults

External fault case	Peak V_{LT} (kV)	t1 (ms)	t2 (ms)	Δt
F1	0.4373	-	-	-
F2	0.4635	-	-	-
F3	0.8969	1.8	-	-
F4	0.4371	-	-	-
F5	16.5601	1	1.1	0.1
F6	6.4552	0.3	0.3	0

Table 5.21: Effect of external faults on DC Reactor Voltage Change Rate-based protection

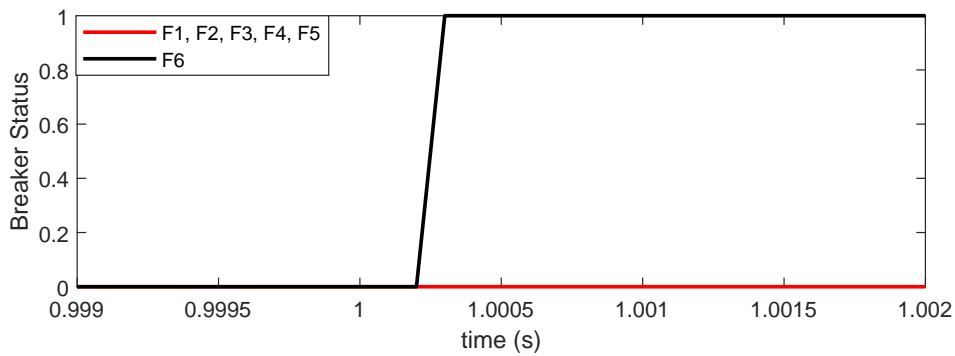


Figure 5.33: Breaker operation for external faults

5.5.5. Effect of Terminal Inductor Inductance

To analyze the effect of the inductance of the terminal inductors on the reactor voltage and the performance of the algorithm, six PTG faults, each having a R_f of 100Ω , located 100km away from R_{131} are triggered. For each fault case, the inductance of the terminal inductors varied from 10 mH to 80 mH. Table 5.22 shows the effect of the trip time due to varied inductance. As the inductance was increased, a decrease in the trip time was observed.

Figure 5.34 shows the effect of varying the inductance of the terminal inductors on the reactor voltage. The peak reactor voltage increases as the inductance is increased. The maximum voltage observed is the highest when the inductance is set at 80 mH. However, as the voltage thresholds, V_{LT1} , and V_{LT2} are crossed within 0.6 ms of the fault, the effect of inductance on the performance of the algorithm is negligible.

Inductance (mH)	Peak V_{LT} (kV)	t1(ms)	t2(ms)	Δt	Trip Time (ms)
10	98.9316	0.5	0.5	0	0.7
20	143.6506	0.5	0.5	0	0.6
40	189.6873	0.5	0.5	0	0.6
60	214.6125	0.5	0.5	0	0.6
80	232.2471	0.5	0.5	0	0.6

Table 5.22: Effect of inductance on DC Reactor Voltage Change Rate-based protection

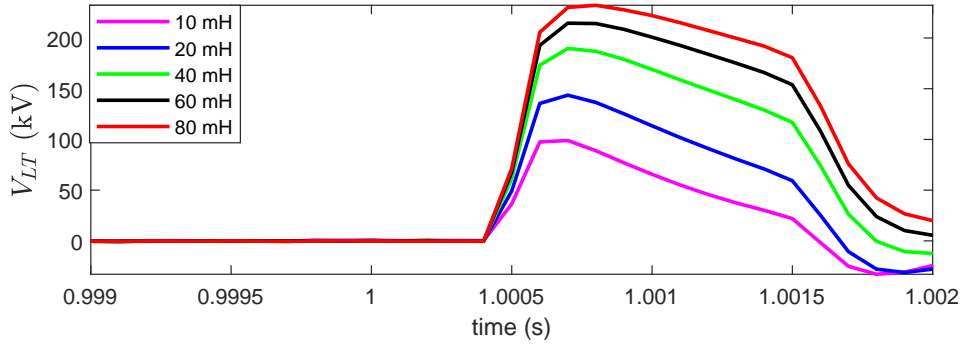


Figure 5.34: V_{LT} during internal faults with varied terminal inductance

5.5.6. Influence Of Noise on Protection Performance

To test the algorithm's resilience against noise, white noise was added to the reactor voltage. The SNR of the noise added was 40 dB. Figure 5.35 shows the resultant reactor voltages after the addition of noise. The thresholds, V_{LT1} and V_{LT2} are crossed only after the fault inception. The Δt observed for was 0 ms. Thus it is evident that the reactor voltage-based algorithm is highly resilient to noise.

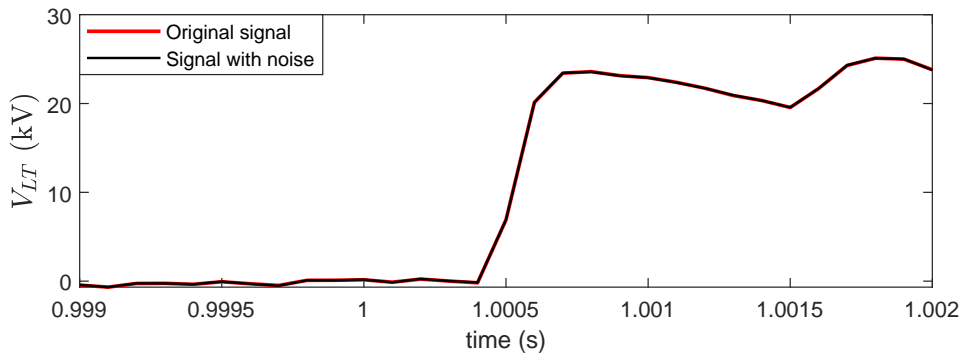


Figure 5.35: V_{LT} with 40 dB noise

5.5.7. Threshold Design

In order for the reactor voltage-based protection to activate, V_{LT2} must be set according to the fault case resulting in the smallest peak V_{LT} . It can be seen that V_{LT} for an NTG fault having R_f set to 200 Ω and x set to 150 km results in the smallest peak V_{LT} , 3.9119 kV. Thus, V_{LT2} should be smaller than 3.9119 kV but bigger than 0.8969 kV. Considering a reliability factor of 1.2, V_{LT2} is set as shown in equation 5.13.

$$V_{LT2} = 1.2 * 0.8969 = 1.07 \text{ kV} \quad (5.13)$$

In this thesis, V_{LT2} has been set as 1.07 kV. In order to set V_{LT1} , the maximum reactor voltage under normal operating conditions is considered. This was found to be 0.4697 kV. Considering a reliability factor of 1.2, V_{LT1} is calculated as shown in equation 5.14 -

$$V_{LT1} = 1.2 * 0.4697 = 0.5636 \text{ kV} \quad (5.14)$$

After multiple simulations of internal and external faults, the threshold for Δt is selected based on the largest Δt recorded for internal faults and the smallest Δt recorded for external faults.

The threshold for Δt should be set such that it is greater than the largest Δt recorded for an internal fault (0 ms), and lesser than the smallest Δt recorded for an external fault (0.1 ms). The external fault resulting in the smallest Δt was the fault case F5. The threshold for Δt was set through according to the Δt recorded for F5. Considering a reliability factor of 1.2, the threshold for Δt was calculated according to (5.15).

$$\Delta t_{thresh} = 0.1/1.2 = 0.0833 \text{ ms} \quad (5.15)$$

5.5.8. Effect of Sampling Frequency

To analyze the effect of the f_s on the performance of the reactor voltage-based protection, a PTG fault ($x = 100 \text{ km}$, $R_f = 200 \Omega$) was simulated at different sampling frequencies. Table 5.23 shows the results of the simulations. It can be seen that as the f_s increases, the trip time decreases. This is due to the faster detection of the crossing of V_{LT1} and V_{LT2} .

f_s (kHz)	Peak V_{LT} (kV)	t1 (ms)	t2 (ms)	Δt (ms)	Trip Time (ms)
10	189.6873	0.5	0.5	0	0.6
20	190.3467	0.5	0.5	0	0.6
50	191.1082	0.4	0.5	0.1	0.56

Table 5.23: Effect of sampling frequency on DC Reactor Voltage Change Rate-based protection

6

Comparison and Analysis

6.1. Summary of HVDC Protection Algorithms Performance

The performance of each algorithm in terms of sensitivity, selectivity, robustness, and speed has been summarized in this section. Each algorithm's performance under various fault conditions, its ability to distinguish various external faults from internal faults, its resilience to noise, and operating speed have been discussed.

6.1.1. Current Differential Deviation

- Sensitivity: The current differential deviation-based algorithm successfully detected PTG, NTG, and PTP faults with a fault resistance of up to 200Ω and fault distances of up to 190 km. As the fault resistance was increased, a decrease in the positive and negative current differential deviations was observed. Furthermore, the algorithm was able to successfully detect internal faults, with the inductance of the current limiting inductors varied from 10 mH to 80 mH. It was observed that the positive and negative current differential deviations were reduced as the inductance was increased. Thus, the current differential deviation-based algorithm offers sufficient sensitivity towards internal faults.
- Selectivity: The protection algorithm was found to successfully discriminate external fault cases such as DC line faults in neighboring cables, AC faults, and remote DC bus faults from internal faults, while the algorithm was falsely triggered for a DC bus fault triggered at Bus 3.
- Speed: The fault resistance was found to have no significant effect on the trip time. The effect of the fault distance on the trip time is much more significant. For PTG and NTG faults, the trip time is seen to decrease as the fault distance approaches the mid-point of the transmission line (100 km). For PTP fault, the trip time increases as the fault distance approaches the mid-point of the transmission line. The protection algorithm was found to have a trip time as low as 0.2 ms, for a PTP fault ($R_f = 200 \Omega$, $x = 10$ km). The longest trip time recorded was 1.2 ms, in the event of a PTG and NTG fault ($R_f = 200 \Omega$, $x = 100$ km). Thus, the current differential deviation-based protection offers high-speed HVDC protection.
- Robustness: To test the noise resilience of the algorithm, white noise with an SNR of 40 dB was added to the current signals measured at R_{13} and R_{31} . It was found that the current differential deviation-based algorithm is able to function accurately in the presence of noise having an SNR of 40 dB or lower. Furthermore, the sampling frequency was varied to test its influence on the protection algorithm. No significant effect was observed on the current differential deviation algorithm due to a change in sampling frequency.

6.1.2. ROCOV

- Sensitivity: The ROCOV-based algorithm was able to detect PTG, NTG and PTP faults with fault resistances of up to 200Ω and fault distances of up to 190 km. To test the sensitivity of the algorithm to the inductance of the current limiting inductors, the performance of the algorithm in the event of a PTG fault with inductance varied from 10 to 80 mH was triggered. It was found that

while $ROCOV_P$ increased as the inductance was increased, $ROCOV_N$ exhibited a decrement in recorded values. However, the algorithm was successfully activated for all inductance values. Thus, the ROCOV-based algorithm offers sufficient sensitivity towards internal faults.

- **Selectivity:** Among the various external fault cases, the ROCOV-based algorithm was found to be able to successfully discriminate external fault cases such as DC line faults in neighboring cables, AC faults, and DC bus faults. The largest $ROCOV_P$ and $ROCOV_N$ recorded for an external fault was 58.14 kV/ms each, while the smallest $ROCOV_P$ and $ROCOV_N$ recorded for an internal fault was 79.0338 kV/ms, and 78.722 kV/ms. The large margin of 20 kV/ms provides an ample margin for ensuring selectivity.
- **Speed:** The protection algorithm was found to have a trip time as low as 0.1 ms for an NTG ($R_f = 200 \Omega$, $x = 10$ km) and PTP fault ($R_f = 200 \Omega$, $x = 10$ km). While the speed of the algorithm was not affected by the fault resistance, varying the fault distance resulted in varying trip times. Particularly, as the fault distance increased, a significant increase in trip time was observed. The shortest trip time recorded was 0.1 ms for an NTG ($R_f = 200 \Omega$, $x = 10$ km) and PTP fault ($R_f = 200 \Omega$, $x = 10$ km), while the longest trip time recorded was 1.2 ms for a PTG fault ($R_f = 200 \Omega$, $x = 190$ km). Thus, the current differential deviation-based protection offers high-speed HVDC protection.
- **Robustness:** To test the noise resilience of the algorithm, white noise with an SNR of 40 dB was added to the positive and negative pole voltage signals measured at R_{31} . It was found that for white noise with an SNR of 40 dB, the ROCOV-based algorithm can still successfully detect internal faults while also being able to differentiate them from external faults. Furthermore, the sampling frequency was varied to test its influence on the protection algorithm. It was observed that as the trip time reduced the sampling frequency increased. Furthermore, the peak $ROCOV_P$ and $ROCOV_N$ observed was increased as the sampling frequency increased.

6.1.3. ROCOC

- **Sensitivity:** The ROCOC-based algorithm was able to detect internal faults with varying fault resistances and fault distances. It was found to successfully detect PTG, NTG, and PTP faults with fault resistances of up to 200Ω . The algorithm was also successfully triggered for fault cases having varied fault distances. The fault distance was varied from 10 km to 190 km. The algorithm was found to successfully detect the internal fault in each case. To test the sensitivity of the algorithm to the inductance of the current limiting inductors, the performance of the algorithm in the event of a PTG fault with inductance varied from 10 to 80 mH was triggered. It was found the $ROCO_C_P$ and $ROCO_C_N$ exhibited a decrement in recorded values. However, the algorithm was successfully activated for all inductance values. Thus, the ROCOC-based algorithm offers sufficient sensitivity towards internal faults.
- **Selectivity:** Among the various external fault cases, the ROCOC-based algorithm was found to be able to successfully discriminate AC faults and remote DC bus faults from internal faults. However, in the event of faults in neighboring cables (F1), and terminal DC bus faults (F5, F6), the algorithm is falsely triggered. Thus the ROCOC-based algorithm offers limited selectivity for HVDC protection.
- **Speed:** While the increase in fault resistance, resulted in slower response, a difference of 0.2 ms was found between the shortest and the longest trip time. The effect of fault distance on the trip time was found to be more significant. The protection algorithm was found to have a trip time as low as 0.1 ms, for a PTP fault ($R_f = 200 \Omega$, $x = 10$ km). However, as fault distance increased, a significant increase in trip time was observed. The longest trip time recorded was 1.2 ms, in the event of a PTG ($R_f = 200 \Omega$, $x = 190$ km), and an NTG fault ($R_f = 200 \Omega$, $x = 190$ km). Thus, the ROCOC-based protection algorithm offers speedy protection action.
- **Robustness:** To test the noise resilience of the algorithm, white noise with an SNR of 40 dB was added to the current signals measured at the positive and negative poles at R_{31} . It was found that the ROCOC-based algorithm was falsely triggered under normal operating conditions and is unable to function accurately in the presence of noise having an SNR of 40 dB or lower. Furthermore, the sampling frequency was varied to test its influence on the protection algorithm. It was observed that as the trip time reduced the sampling frequency increased. Furthermore, the peak $ROCO_C_P$ and $ROCO_C_N$ observed was increased as the sampling frequency increased.

6.1.4. DC Reactor Voltage Change Rate

- **Sensitivity:** The reactor voltage-based algorithm was able to detect internal faults with varying fault resistances and fault distances. It was found to successfully detect PTG, NTG, and PTP faults with fault resistances of up to 200Ω and fault distances of up to 190 km. The algorithm was found to successfully detect the internal fault in each case. To test the sensitivity of the algorithm to the inductance of the current limiting inductors, the performance of the algorithm in the event of a PTG fault with inductance varied from 10 to 80 mH was triggered. It was found that the V_{LT} recorded exhibited an increase as the inductance was increased. However, no change in Δt , t_1 , and t_2 was observed. Nevertheless, the reactor voltage-based algorithm was successfully activated for all inductance values. Thus, the Reactor voltage-based algorithm offers sufficient sensitivity towards internal faults.
- **Selectivity:** Among the various external fault cases, the Reactor voltage-based algorithm was found to be able to successfully discriminate internal faults from DC faults in neighboring lines, AC faults, and remote DC bus faults. However, in the event of DC bus faults at the terminal of the protected line (F6), the algorithm is falsely triggered. Thus the selectivity of the reactor voltage algorithm is limited by DC bus faults.
- **Speed:** While the fault resistance did not have much effect on t_1 , t_2 , or the trip time, the fault distance had a significant effect on the same. As the fault distance was increased, t_1 , t_2 , and the trip time were found to increase. This can be attributed to the fact that as the reactor voltage takes more time to cross voltage thresholds V_{LT1} (t_1) and V_{LT2} (t_2), the algorithm will take longer to be activated. The protection algorithm was found to have a trip time as low as 0.2 ms for a PTP fault ($R_f = 200 \Omega$, $x = 10$ km). However, as fault distance increased, a significant increase in trip time was observed. The longest trip time recorded was 1.2 ms, in the event of a PTG ($R_f = 200 \Omega$, $x = 190$ km), and an NTG fault ($R_f = 200 \Omega$, $x = 190$ km). Thus, the Reactor voltage-based protection algorithm offers speedy protection action.
- **Robustness:** To test the noise resilience of the algorithm, white noise with an SNR of 40 dB was added to the measured voltage across the positive pole current limiting inductor at R_{31} . It was found that the reactor voltage was unaffected by white noise having an SNR of 40 dB or lower.

6.2. Inferences

In this thesis, four HVDC protection algorithms have been discussed. These were the current differential deviation-based protection, ROCOV-based protection, ROCOC-based protection, and reactor voltage change rate-based protection. The sensitivity of all algorithms was seen to decrease with the increase in fault resistance. The performance of all algorithm's sensitivity has been summarized in Table 6.1. While all four protection algorithms work accurately for fault resistances of up to 200Ω , increasing the fault resistance further will result in a compromise between selectivity and sensitivity. If the threshold is set too high, the protection will not be triggered for faults with high fault resistances, compromising its sensitivity. However, if the threshold is set too low, the algorithm will generate a trip signal for external faults as well, compromising its selectivity. The effect of increasing the inductance of the current limiting inductors on the DC line implied an increase or decrease in the threshold setting for the different algorithms. For the current differential deviation-based algorithm, the ROCOC-based algorithm, and the ROCOV-based algorithm the threshold would have to be reduced. While the voltage thresholds for V_{LT1} , and V_{LT2} would have to be increased for the reactor voltage change rate-based algorithm. While all HVDC protection algorithms were successfully triggered for all internal fault cases, thereby assuring sufficient sensitivity, the selectivity against various external faults was found to be different for each protection. These have been summarized in Table 6.1.

As the fault distance was increased, the speed of operation for the ROCOV-based, ROCOC-based, and reactor voltage change rate-based algorithms was found to have increased. For the current differential deviation-based algorithm, the speed of operation of the algorithm was found to have increased as the fault distance was increased for PTG and NTG faults, the longest trip time was found to be for faults located in the middle of the transmission line. Thus, all protection algorithms' operation speeds are found to be dependent on the fault distance, and while their operating speed is sufficient for a 200 km line in this model, lines longer than this will result in an operation speed longer than the required speed of 2 ms [30]. The performance of each algorithm has been summarized in Table 6.1

The addition of 40 dB SNR white noise to the input signals for the different HVDC protection algo-

rithms provided insight into the robustness of the algorithms. While the current differential deviation-based protection and the ROCOV-based protection operated successfully, it can be seen that for noise with a lower SNR, these algorithms will be activated under normal operating conditions with the current thresholds. The threshold for the ROCOC-based algorithm was crossed under normal operating conditions after the addition of noise in the input current signals, thus the ROCOC-based algorithm is not sufficiently robust against noise of 40 dB or lower. The reactor voltage change rate-based algorithm was found to be the most robust to noise among all the four algorithms investigated. It was found that there is minimal change in the reactor voltage signal when noise is added to it. The results of the robustness analysis of each algorithm have been summarized in Table 6.1

	Current differential deviation	ROCOV	ROCOC	DC reactor voltage
Sensitivity				
R_f : 0 Ω to 200 Ω	Y	Y	Y	Y
x : 10km to 190 km	Y	Y	Y	Y
Selectivity				
F1 (PTP fault in neighbouring line)	N	N	Y	N
F2 (AC fault)	N	N	N	N
F3 (AC fault)	N	N	N	N
F4 (Remote bus fault)	N	N	N	N
F5 (DC bus fault)	Y	N	Y	N
F6 (DC bus fault)	N	N	Y	Y
Speed				
Shortest trip time	0.2 ms	0.1 ms	0.1 ms	0.2 ms
Longest trip time	1.2 ms	1.2 ms	1.2 ms	1.2 ms
Robustness				
Resilient to 40 dB noise	Y	Y	N	Y

Table 6.1: HVDC protection performance summary

7

Conclusion and Future Work

7.0.1. Conclusion

In the past two decades from 2000, the rapid development of the HVDC system benefits from the increases in the market share of renewable energy and the revolution of the power converter technologies. However, there is no globalized protection standard for HVDC systems as it is in traditional AC grids. The protection strategy and protection still vary around the world. This thesis aimed to evaluate and review the protection algorithms dedicated to fault detection in HVDC lines. In Chapter 1, the HVDC system is introduced, outlining its benefits and advantages over traditional AC systems. The protection of these HVDC systems forms a crucial aspect of its development. Thus, this thesis aims to achieve the following research objectives:

- Implementing protection algorithms in PSCAD
- Investigate how various fault parameters affect the performance of each algorithm
- Determination of the optimal threshold values for each algorithm
- Analyze the algorithms' performance in terms of selectivity, sensitivity, reliability, and speed.

Chapter 2 briefly describes the test system used for testing the protection algorithm. The CIGRE B4-57 4 terminal model has been used for this purpose. Chapter 3 discusses various existing HVDC protection algorithms along with their advantages and disadvantages. All HVDC protection algorithms can be broadly classified into single-ended protection or double-ended protection depending on the requirement of a communication channel. The double-ended protection algorithms require a communication channel to exchange fault data, while single-ended protection algorithms are free from this requirement. The existing double-ended protection algorithms can be classified into two categories. These are -

- Differential protection
- Directional protection

Furthermore, single-ended protection is preferred as the primary protection due to its higher speed and improved selectivity. The single-ended algorithms are further classified depending on the fault data used. Primarily, these are -

- Overcurrent/Undervoltage based-algorithms
- Current/Voltage derivative-based algorithms
- Boundary reactor-based algorithms
- Time-domain TW-based-algorithms
- Frequency domain-based algorithms

This thesis evaluates four HVDC protection algorithms. These are -

- Current differential deviation-based protection
- ROCOV-based protection
- ROCOC-based protection
- DC reactor voltage change rate-based protection

Chapter 4 discussed these algorithms in detail. The current differential deviation-based protection utilizes the rate of change of the differential current in the positive and negative poles of the protected line to form the protection. The ROCOC and ROCOV-based methods utilize the rate of change of current and voltage respectively in the positive and negative poles of the protected line. Finally, the rate of change of reactor voltage-based protection utilizes the time taken for the positive pole reactor voltage to cross set voltage thresholds.

Chapter 5 discusses the simulation results observed while testing the algorithms in the PSCAD environment. All four algorithms were implemented in the PSCAD environment. Additionally, MATLAB was used to perform the noise resilience analysis of each algorithm. The performance of each algorithm under internal faults and external faults was studied to determine the selectivity of the algorithm. The fault resistance, R_f , and fault distance, x were varied to test the sensitivity of each algorithm under varied fault scenarios. Furthermore, the effect of varying the inductance of the current limiting inductors and varying the sampling frequency on each algorithm was studied. The speed of each algorithm was monitored by observing the trip time of the single-phase breakers on the protected line. The threshold-determining process has been described for each algorithm as well. Lastly, the robustness of each algorithm was tested by adding Gaussian white noise having an SNR of 40 dB to the input signals of each algorithm and testing the algorithm's performance. Finally, Chapter 6 discusses the performance of each algorithm in terms of speed, selectivity, sensitivity, and robustness.

This thesis aimed to answer the following research questions -

- **How can DC faults be detected in a fast and accurate way?** - In terms of speed, the voltage-based algorithms (ROCOV, Reactor voltage) resulted in a shorter trip time than the current-based algorithms (Current differential deviation, ROCOC). To ensure accuracy, the threshold setting must be calibrated properly. Multiple internal and external fault scenarios need to be simulated, following which the corresponding fault-determining parameter ($ROCOV_P$, $ROCOV_N$ in the ROCOV-based method) is recorded. The threshold must be set in a way that it detects the internal fault resulting in the smallest recorded fault-determining parameter.
- **How can the protection's selectivity be ensured?** The threshold setting should be set such that it remains idle for the external fault resulting in the recording of the largest fault-determining parameter. To ensure selectivity, the fault-determining parameter should be able to distinguish internal faults from external faults with an error-free margin. As in the ROCOV-based method, the smallest internal fault to be detected had a resulting maximum $|ROCOV|$ of 78 kV/ms, while the largest external fault resulted in a maximum $|ROCOV|$ of 59.31 kV/ms. Thus the threshold setting having a large margin of 18.69 kV/ms ensures the selectivity of the algorithm.

7.0.2. Future Work

While this thesis evaluated the performance of the protection algorithms under varied fault scenarios, the work done in this thesis can be developed further by testing multiple fault types for the external fault case F1. Furthermore, frequency-based methods such as HHT-based protection or ST-based protection can be analyzed using this methodology.

References

- [1] ABB. *Introducing HVDC*. 2014.
- [2] Mesut E. Baran and Nikhil R. Mahajan. "Overcurrent Protection on Voltage-Source-Converter-Based Multiterminal DC Distribution Systems". In: *IEEE Transactions on Power Delivery* 22.1 (2007), pp. 406–412.
- [3] Rui Bertho et al. "Selective Nonunit Protection Technique for Multiterminal VSC-HVDC Grids". In: *IEEE Transactions on Power Delivery* 33.5 (2018), pp. 2106–2114.
- [4] Hadi Dadgostar, Masood Hajian, and Khaled Ahmed. "DC grids DC fault detection using asymmetric pole inductors". In: *Electric Power Systems Research* 193 (2021), p. 107016.
- [5] Ghazal Falahi et al. "Design, Modeling and Control of Modular Multilevel Converter based HVDC Systems." In: (2014).
- [6] Ghazal Falahi and Alex Q Huang. "Design consideration of an MMC-HVDC system based on 4500V/4000A emitter turn-off (ETO) thyristor". In: *2015 IEEE Energy Conversion Congress and Exposition (ECCE)*. IEEE. 2015, pp. 3462–3467.
- [7] Shu-ping Gao, Qi Liu, and Guo-bing Song. "Current differential protection principle of HVDC transmission system". In: *IET Generation, Transmission & Distribution* 11.5 (2017), pp. 1286–1292.
- [8] Teymoor Ghanbari and Ebrahim Farjah. "Development of an efficient solid-state fault current limiter for microgrid". In: *IEEE Transactions on Power Delivery* 27.4 (2012), pp. 1829–1834.
- [9] J. Grainger and W. Stevenson. *Power System Analysis*. McGraw-Hill, 1994.
- [10] Mehr Gul et al. "Technical and Economic Assessment of VSC-HVDC Transmission Model: A Case Study of South-Western Region in Pakistan". In: *Electronics* 8 (Nov. 2019), p. 1305.
- [11] HengXu Ha et al. "Novel scheme of travelling wave based differential protection for bipolar HVDC transmission lines". In: *2010 International Conference on Power System Technology*. 2010, pp. 1–6.
- [12] Masood Hajian, Lu Zhang, and Dragan Jovcic. "DC transmission grid with low-speed protection using mechanical DC circuit breakers". In: *IEEE Transactions on Power Delivery* 30.3 (2014), pp. 1383–1391.
- [13] T Halder. "Comparative study of HVDC and HVAC for a bulk power transmission". In: *2013 International Conference on Power, Energy and Control (ICPEC)*. IEEE. 2013, pp. 139–144.
- [14] Naushath M Haleem and Athula D Rajapakse. "Fault-type discrimination in HVDC transmission lines using rate of change of local currents". In: *IEEE Transactions on Power Delivery* 35.1 (2019), pp. 117–129.
- [15] Bjorn Jacobson et al. "VSC-HVDC transmission with cascaded two-level converters". In: *Proc. Cigre* (2010), B4–B110.
- [16] Dragan Jovcic, Lu Zhang, and Masood Hajian. "LCL VSC Converter for High-Power Applications". In: *IEEE Transactions on Power Delivery* 28.1 (2013), pp. 137–144.
- [17] Amir Kalantari et al. "Natural frequency based protection for star-connected multiterminal VSC-HVDC transmission lines". In: *Conference on Recent Research in Science and Technology*. 2017.
- [18] Ali Khaleghi-Abbasabadi, Mohammad Mehrabi-Kooshki, and Sadegh Jamali. "A Protection Scheme for Multi-Terminal HVDC Grids Using Local Transient Voltage Characteristics". In: *2023 International Conference on Protection and Automation of Power Systems (IPAPS)*. IEEE. 2023, pp. 1–7.
- [19] Prabha Kundur. "Power system stability". In: *Power system stability and control* 10 (2007), pp. 7–1.

- [20] P. Rey L. Zhang L. Harnefors. "Power System Reliability and Transfer Capability Improvement by VSC-HVDC (HVDC Light®)". In: *CIGRE 2007 Conference on Security and Reliability of Electric Power Systems* 18 (2007), p. 20.
- [21] Willem Leterme, Jef Beerten, and Dirk Van Hertem. "Nonunit protection of HVDC grids with inductive DC cable termination". In: *IEEE Transactions on Power Delivery* 31.2 (2015), pp. 820–828.
- [22] Aimin Li et al. "Study on the dynamic performance characteristics of HVDC control and protections for the HVDC line fault". In: *2009 IEEE Power & Energy Society General Meeting*. IEEE. 2009, pp. 1–5.
- [23] Chengyu Li, Aniruddha M. Gole, and Chengyong Zhao. "s". In: *IEEE Transactions on Power Delivery* 33.5 (2018), pp. 2254–2264.
- [24] Rui Li and Lie Xu. "Review of DC fault protection for HVDC grids". In: *WIREs Energy and Environment* 7.2 (2018), e278.
- [25] Rui Li, Lie Xu, and Liangzhong Yao. "DC fault detection and location in meshed multiterminal HVDC systems based on DC reactor voltage change rate". In: *IEEE Transactions on Power Delivery* 32.3 (2016), pp. 1516–1526.
- [26] Yan Li, Yanfeng Gong, and Bin Jiang. "A novel traveling-wave-based directional protection scheme for MTDC grid with inductive DC terminal". In: *Electric Power Systems Research* 157 (2018), pp. 83–92.
- [27] Zhen-qiang Li and Yan-ping Lv. "A Novel Scheme of HVDC Transmission Line Voltage Traveling Wave Protection Based on Wavelet Transform". In: *2008 International Conference on High Voltage Engineering and Application*. 2008, pp. 163–167.
- [28] Érica Manguera Lima, Núbia Silva Dantas Brito, and Benemar Alencar de Souza. "High impedance fault detection based on Stockwell transform and third harmonic current phase angle". In: *Electric Power Systems Research* 175 (2019), p. 105931. ISSN: 0378-7796.
- [29] Le Liu, Aleksandra Lekić, and Marjan Popov. "Robust Traveling Wave-Based Protection Scheme for Multiterminal DC Grids". In: *IEEE Transactions on Power Delivery* (2023).
- [30] Lian Liu. "Protection of multi-terminal HVDC systems: Algorithm development and performance verification by EMT simulations". In: (2019).
- [31] Xiaolei Liu, AH Osman, and OP Malik. "Stationary wavelet transform based HVDC line protection". In: *2007 39th North American Power Symposium*. IEEE. 2007, pp. 37–42.
- [32] Zhou Liu et al. "Protection testing for multiterminal high-voltage dc grid: Procedures and procedures and assessment". In: *IEEE Industrial Electronics Magazine* 14.3 (2020), pp. 46–64.
- [33] Willis Long and Stig Nilsson. "HVDC transmission: yesterday and today". In: *IEEE Power and Energy Magazine* 5.2 (2007), pp. 22–31.
- [34] Shuxin Luo et al. "A directional protection scheme for HVDC transmission lines based on reactive energy". In: *IEEE transactions on Power Delivery* 31.2 (2015), pp. 559–567.
- [35] N.M. MacLeod et al. "A new 500MW back - to - back station to provide power exchange between Uruguay and Brazil". In: *9th IET International Conference on AC and DC Power Transmission (ACDC 2010)*. 2010, pp. 1–5.
- [36] J. I. Marvik, S. D'Arco, and J. A. Suul. "Communication-less fault detection in radial multi-terminal offshore HVDC grids". In: *11th IET International Conference on AC and DC Power Transmission*. 2015, pp. 1–8.
- [37] JI Marvik, S D'Arco, and JA Suul. "A two-layer detection strategy for protecting multi-terminal HVDC systems against faults within a wide range of impedances". In: *13th International Conference on Development in Power System Protection 2016 (DPSP)*. IET. 2015, pp. 1–6.
- [38] Pannala Krishna Murthy et al. "Wavelet transform approach for detection and location of faults in HVDC system". In: *2008 IEEE Region 10 and the Third international Conference on Industrial and Information Systems*. IEEE. 2008, pp. 1–6.

- [39] Ryoya Ota et al. "DC fault detection method using current differential deviation in MTDC grid". In: *2018 IEEE PES Asia-Pacific Power and Energy Engineering Conference (APPEEC)*. IEEE. 2018, pp. 139–142.
- [40] Maria Jose Perez-Molina et al. "A comparison of non-unit and unit protection algorithms for HVDC grids". In: *2019 AEIT HVDC International Conference (AEIT HVDC)*. IEEE. 2019, pp. 1–6.
- [41] María José Pérez-Molina et al. "Non-unit ROCOV scheme for protection of multi-terminal HVDC systems". In: *2020 22nd European Conference on Power Electronics and Applications (EPE'20 ECCE Europe)*. 2020, pp. 1–10.
- [42] Vasileios Psaras et al. "Non-Unit Protection for HVDC Grids: An Analytical Approach for Wavelet Transform-Based Schemes". In: *IEEE Transactions on Power Delivery* 36.5 (2021), pp. 2634–2645.
- [43] Vasileios Psaras et al. "Review and Evaluation of the State of the Art of DC Fault Detection for HVDC Grids". In: *2018 53rd International Universities Power Engineering Conference (UPEC)*. 2018, pp. 1–6.
- [44] Reza Rohani and Amangaldi Koochaki. "A Hybrid Method Based on Optimized Neuro-Fuzzy System and Effective Features for Fault Location in VSC-HVDC Systems". In: *IEEE Access* 8 (2020), pp. 70861–70869.
- [45] P. Routray, M. Mishra, and P.K. Rout. "High Impedance Fault detection in radial distribution system using S-Transform and neural network". In: *2015 IEEE Power, Communication and Information Technology Conference (PCITC)*. 2015, pp. 545–551.
- [46] Umar Saleem et al. "Faults detection and classification of HVDC transmission lines of using discrete wavelet transform". In: *2018 International Conference on Engineering and Emerging Technologies (ICEET)*. IEEE. 2018, pp. 1–6.
- [47] Khaled A. Saleh et al. "Protection of High-Voltage DC Grids Using Traveling-Wave Frequency Characteristics". In: *IEEE Systems Journal* 14.3 (2020), pp. 4284–4295.
- [48] Siemens. *Fact sheet High-voltage direct current transmission (HVDC)*. 2012.
- [49] Kundan Singh and Abhisek Ukil. "Fault Detection in HVDC Transmission Line by S-Transform Technique". In: *2019 IEEE PES Asia-Pacific Power and Energy Engineering Conference (APPEEC)*. 2019, pp. 1–5.
- [50] Jeremy Sneath and Athula D Rajapakse. "Fault detection and interruption in an earthed HVDC grid using ROCOV and hybrid DC breakers". In: *IEEE Transactions on Power Delivery* 31.3 (2014), pp. 973–981.
- [51] Jeremy Sneath and Athula D. Rajapakse. "DC Fault Protection of a Nine-Terminal MMC HVDC Grid". In: *11th IET International Conference on AC and DC Power Transmission*. 2015, pp. 1–8.
- [52] Ying Song, Gaoyang Hou, and Song Wang. "DC Fault Detection Method for DC Grids Based on Frequency Domain Voltage Characteristics". In: *2021 6th International Conference on Power and Renewable Energy (ICPRE)*. 2021, pp. 196–201.
- [53] P. Srikanth, A. K. Chandel, and K. A. Naik. "HVDC system fault identification using S-transform approach". In: *2010 International Conference on Power, Control and Embedded Systems*. 2010, pp. 1–6.
- [54] Xiaoyun Sun, Xiangqian Tong, and Jun Yin. "Fault Diagnosis for VSC-HVDC Using Wavelet Transform". In: *2012 Asia-Pacific Power and Energy Engineering Conference*. 2012, pp. 1–4.
- [55] Ning Tong et al. "Local Measurement-Based Ultra-High-Speed Main Protection for Long Distance VSC-MTDC". In: *IEEE Transactions on Power Delivery* 34.1 (2019), pp. 353–364.
- [56] Raymundo E Torres-Olguin and Hans Kristian Høidalen. "Inverse time overcurrent protection scheme for fault location in multi-terminal HVDC". In: *2015 IEEE Eindhoven PowerTech*. IEEE. 2015, pp. 1–6.
- [57] Wang Xiang et al. "DC fault protection algorithms of MMC-HVDC grids: Fault analysis, methodologies, experimental validations, and future trends". In: *IEEE Transactions on Power Electronics* 36.10 (2021), pp. 11245–11264.

-
- [58] Huangqing Xiao et al. "Operation and control of hybrid HVDC system with LCC and full-bridge MMC connected in parallel". In: *IET Generation, Transmission & Distribution* 14.7 (2020), pp. 1344–1352.
- [59] Jin Yang, John E. Fletcher, and John O'Reilly. "Short-Circuit and Ground Fault Analyses and Location in VSC-Based DC Network Cables". In: *IEEE Transactions on Industrial Electronics* 59.10 (2012), pp. 3827–3837.
- [60] Saizhao Yang et al. "An Improved DC Fault Protection Algorithm for MMC HVDC Grids Based on Modal-Domain Analysis". In: *IEEE Journal of Emerging and Selected Topics in Power Electronics* 8.4 (2020), pp. 4086–4099.
- [61] Chenhao Zhang et al. "Single-ended traveling wave fault location method in DC transmission line based on wave front information". In: *IEEE Transactions on Power Delivery* 34.5 (2019), pp. 2028–2038.
- [62] S. Zhang et al. "Realization of the transient-based boundary protection for HVDC transmission lines based on high frequency energy criteria". In: *2010 International Conference on Power System Technology*. 2010, pp. 1–7.
- [63] Xiaodong Zheng et al. "Harmonic current protection scheme for voltage source converter-based high-voltage direct current transmission system". In: *IET Generation, Transmission & Distribution* 8.9 (2014), pp. 1509–1515.
- [64] Guibin Zou et al. "A fast protection scheme for VSC based multi-terminal DC grid". In: *International Journal of Electrical Power & Energy Systems* 98 (2018), pp. 307–314.